Parameterization adaption needed to unlock the benefits of increased resolution for the ITCZ in ICON

Clarissa A. Kroll[1], Robert C. Jnglin Wills[1], Luis Kornblueh[2], Ulrike Niemeier[2], and
Andrea Schneidereit[3]

[1]Institute for Atmospheric and Climate Science, ETH Zürich, Zürich, Switzerland
[2]Max Planck Institute for Meteorology, Hamburg, Germany
[3]Deutscher Wetterdienst, Offenbach am Main, Germany

Correspondence: Clarissa A. Kroll (clarissa.kroll@env.ethz.ch)

Abstract. The double Inter-Tropical Convergence Zone (~~dITCZ) is a prominent precipitation bias persistent over several~~ double-ITCZ) bias is a persistent tropical precipitation bias over many climate model generations. This motivates investigations of whether increasing resolution and discarding ~~parametrizations can improve~~ parameterizations improves the representation of the large-scale atmospheric circulation and ITCZ. In this work, we ~~use the unique possibility offered by the new ICON XPP model configuration to study the dITCZ bias in a~~ study the double-ITCZ bias in an ICON XPP resolution hierarchy spanning from parameterized to ~~resolved~~ explicitly described deep convection within a consistent ~~modeling~~ framework. We demonstrate that the ~~dITCZ persists from a horizontal resolution of~~ double-ITCZ persists across horizontal resolutions from 160 km ~~up~~ to 5 km in specified ~~sea surface temperature simulationsand is independent of the~~ sea-surface temperature simulations, independent of deep-convective and non-orographic gravity wave ~~parametrization~~parameterization. Changes in the treatment of near-surface wind speed within the ~~bulk flux formula~~ turbulence parameterization can reduce the ~~dITCZ biasover the resolution hierarchy. We however highlight that the root cause of the dITCZ lies in biased~~ bias. However, we highlight that a key driver of the double-ITCZ bias in ICON seems to lie in the insufficient moisture transport from the subtropics to the inner tropics. The resulting low bias in tropical near-surface moisture ~~substantially~~ reduces deep convection over the Warm Pool, leading to a weakened Walker ~~Circulation~~circulation. These biases ultimately culminate in the ~~dITCZ feature. An increase in~~ double-ITCZ feature. Increasing the near-surface wind speed ~~addresses the low bias in~~ limiter improves tropical near-surface moisture ~~in the tropics, however it exacerbates a~~ but exacerbates the bias in the moisture source~~by~~ , increasing the inner tropical ~~over the subtropical contribution . This could endanger~~ contribution at the expense of the subtropics. This degrades the representation of the global circulation, ~~energetic balance~~energy balance, and teleconnections. Additionally, we show that parameter adjustments at low resolution are informative of the response to the same parameter adjustments at high resolution. Our findings showcase the benefits of models supporting a range of resolutions and underline the importance of continuing the development of ~~non-discardable parametrizations.~~ non-discardible parameterizations.

1 Introduction

The hydrological cycle is an important manifestation of the global atmospheric circulation~~and plays a key role in Earth's energy budget. The Inter-Tropical Convergence Zone (ITCZ) is at the center of the meridional circulation which imports moisture into the tropics and exports energy to higher latitude .~~. Despite its importance, biases in the representation of precipitation within the ~~ITCZ~~ Inter-Tropical Convergence Zone (ITCZ) have been a persistent challenge throughout many model generations in the Coupled Model Intercomparison Project ~~, CMIP~~(CMIP) (Tian and Dong, 2020). Among them, the double-ITCZ bias ~~(dITCZ), i.e., the tendency to overestimate precipitation over ocean in the southern tropics and underestimate it at the equator,~~ is the most prominent problem ~~. Since the impacts of the~~ (Mechoso et al., 1995; Lin, 2007). It describes positive precipitation biases south of the equator in the eastern Pacific and Atlantic, as well as underestimated precipitation in the equatorial Pacific. While observations indicate that a double-ITCZ ~~are relevant beyond the ocean regions in which it occurs, influencing the El Niño-Southern Oscillation and other large-scale climate phenomena, the origin of this bias has been central to the precipitation bias discussions.~~

~~When speaking of the dITCZ, it is important to note that the dITCZ is not an entirely artificial phenomenon which is only seen in climate simulations. In fact observations indicate the dITCZ can also occur naturally~~ feature can occur naturally in these regions at certain times of the year, preferentially in March ~~. The problem is therefore not the appearance of the dITCZ as such but that it is~~ (Magnusdottir and Wang, 2008; Gonzalez et al., 2025), these features are much too strong and ~~persists throughout the year~~ persistent in model simulations. ~~Over the Pacific, the natural dITCZ feature is associated with local minima in surface humidity and temperature along the equator or increased wind convergence~~ In addition to its influence on regional precipitation biases, the double ITCZ can influence large-scale climate phenomena such as the El Niño-Southern Oscillation (Ham and Kug, 2014; Zhang et al., 2014). Therefore, identifying the cause of the double ITCZ is a key step towards improving climate models.

In order to understand the simulated ~~year-long dITCZ bias,~~ double-ITCZ bias, it is helpful to consider the role of the ITCZ ~~in the earth system has to be studied. The ITCZ is part of the global system of energy redistribution, which in the atmosphere is largely handled by the~~ at the center of the large-scale ~~meridional circulation.~~ atmospheric meridional circulation that imports moisture into the tropics and exports energy to higher latitudes (Holton, 2004; Schneider et al., 2014). Subtropical moisture is transported within the ~~Trade Winds~~ trade winds into the inner tropics, ~~fueling the hydrological cycle. This supply of moisture from higher latitudes leads to the well-known excess of precipitation over evaporation caused moisture mass flux in the tropics. The moisture import into the tropics is then balanced by an energy export to the subropics, with the ITCZ at the center of the corresponding meridional circulation,~~ where its convergence sustains the ITCZ (Peixoto and Oort, 1992). The moist static energy content is greater in the poleward return flow in the upper troposphere, such that there is a net energy transport into the subtropics by the Hadley cells (Figure 1a). Since the position and structure of the ITCZ and ~~distribution of~~ the distribution of the net energy input to the atmosphere are interrelated (Bischoff and Schneider, 2014; Ren and Zhou, 2024), changes in the distribution of precipitation will be reflected in the atmospheric energy budget ~~,~~ and vice versa. For example, the ITCZ resides in the Northern Hemisphere in the annual-mean due to the difference in the net energy input between the Northern and Southern Hemispheres ~~. In an energetically motivated framework, precipitation biases can be separated into hemispherically symmetrical and asymmetrical components . The symmetric component is related to the net energy input near the equator and the anti-symmetric component to cross-equatorial energy flux, which again is influenced by asymmetries in the net energy input in the two hemispheres~~(Philander et al., 1996; Frierson et al., 2013; Marshall et al., 2014). This underlines that the ~~dITCZ~~ double-ITCZ problem cannot be investigated as an isolated tropical phenomenon~~, since subtropical~~ : Sub- and extratropical biases in the energy budget can also be sources of the problem (Kang et al., 2008; Hwang and Frierson, 2013; Kang et al., 2019), and tropical biases can likewise cause biases in the ~~subtropics~~ sub- and extratropics (Henderson et al., 2017; Dong et al., 2022; Feng et al., 2023).

~~This~~

It is critical to recognize the coupling between the ~~dITCZ~~ double-ITCZ problem and biases in the energy budget ~~is critical in recognizing~~ also in the context of model tuning, because the first ~~model evaluation step is – most naturally –~~ step of model evaluation is in many cases the energy balance of the model (Wild, 2020). Most model evaluation workflows focus first on global mean top-of-the-atmosphere (TOA) fluxes and potentially surface energy fluxes (Mauritsen et al., 2012), ~~with the understanding that modelers will then~~ and then proceed to tune additional atmospheric fields and processes, for example, as outlined in ~~Hourdin et al. 2017~~ Hourdin et al. (2017). This is done with the knowledge that there can be trade-offs between these different optimizations, making dedicated approaches to optimize across multiple processes necessary, for example to focus on the precipitation distribution and TOA fluxes within one framework (Zhao et al., 2018a, b). However, in general, most published model evaluation workflows provide little information on ~~the~~ regional energy budgets that are mechanistically important for the large-scale circulation and ~~the distribution of precipitation~~ precipitation distribution. This poses a problem: ~~sometimes improvements in global-mean~~ Sometimes improvements in global mean energy fluxes introduce compensating errors in regional energy fluxes and lead to deterioration of the large-scale circulation and precipitation distribution.

Next to model tuning choices~~which disregard the impact on the large-scale circulations~~, an additional possible source of tropical precipitation biases is the incorrect representation of convective processes in coarse-scale models. Discarding potentially error-prone convective ~~parametrizations~~ parameterizations (Arakawa, 2004; Jones and Randall, 2011; Sherwood et al., 2014; Hardiman et al., 2015) has therefore been one of the avenues explored to address ~~this problem~~ the double-ITCZ problem (Song and Zhang, 2018; Zhou et al., 2022; Ma et al., 2023). In this context, it is important to note that even at a horizontal resolution of 5 km, the necessity of deep convective parameterizations is still disputed, with some studies showing improvements in atmospheric representation with the elimination of parameterizations (Vergara-Temprado et al., 2020) and others showing deterioration and insufficiently resolved processes (Clark et al., 2024). Additionally, although it is ~~often~~ sometimes stated that high-resolution simulations are less sensitive to ~~parametrization~~ parameterization choices than low-resolution simulations, ~~some parametrizations~~ a number of parameterizations still remain – such as the cloud microphysics, non-orographic gravity wave, turbulence, and in some cases shallow convective ~~parametrizations~~ parameterizations – all of which are ~~of importance~~ important for the model~~energetics~~ 's atmospheric circulation and energy budget (Hu et al., 2021; Hájková and ácha, 2023). High computational costs, in combination with the ~~misconception that all~~ hope that the most relevant processes are now resolved, ~~often~~ can however then lead to a ~~substantial~~ shortening of the model tuning process in high-resolution simulations. ~~Therefore, the~~ A lack of systematic tuning could be one of the reasons why high-resolution ~~convection-resolving simulations without parametrizations~~ convection-permitting simulations without parameterizations do not show improvements in skill for the tropical precipitation pattern compared to conventional CMIP models, ~~whereas~~ while high-resolution simulations ~~still relying on parametrization~~ that still rely on parameterization can outperform both (Zhou et al., 2022; Schneider et al., 2024).

In this work, we investigate the precipitation distribution and the ~~dITCZ~~ double-ITCZ bias in a resolution hierarchy of the ICON model spanning from ~~parametrization supported~~ parameterization-supported 160 km to ~~deep-convection resolving~~ deep-convection-permitting 5 km horizontal resolution. We ~~outline~~ discuss the influence of modeling parameter choices over the resolution hierarchy, using an otherwise identical setup, model code, and boundary conditions ~~,~~ to allow for a robust ~~and fair~~ comparison. This endeavor has only ~~recently been made possible within the ICON XPP configuration~~ been recently enabled by the newly developed XPP configuration of the ICON climate model (Früh et al., 2022; Niemeier et al., 2023; Müller et al., 2024)~~which~~ , which can be run efficiently employing GPUs at a wide range of horizontal resolutions and, in contrast to ICON sapphire (Hohenegger et al., 2022), supports the usage of convective ~~parametrizations in ICON~~parameterizations. We focus on ~~three leading~~ the following questions:

1. **Resolution and parameterization dependence of the double-ITCZ bias:** Can increased horizontal resolution and ~~the discard of~~ switching off deep convective and gravity wave ~~parametrization resolve the dITCZ~~ parameterization improve the double-ITCZ bias? Are there common biases across resolutions? Where can resolution-dependent improvements be found?
   (*Addressed in Section 3.1 and 3.3*)

2. **Resolution-(in)dependent bias corrections:** To the extent that there are common (~~dITCZ~~double-ITCZ) biases, how can they be addressed and can the same adjustments be applied at various resolutions?
   (*Addressed in Section 3.2 and 3.3*)

3. **Underlying mechanisms:** What are the underlying mechanisms leading to the ~~dITCZ biases~~ double-ITCZ bias in ICON and how do the chosen adjustments ameliorate it?
   (*Addressed in Section 3 and Section 4, summarized in ~~Fig 12~~Schematic Figure 1*)

To address the second ~~research question~~group of research questions, we focus on the choice of a minimum surface wind speed threshold ~~in the bulk-flux formulation. Mechanistically, following the bulk flux formula, a higher~~ (U_{min}~~leads to an increased latent heat flux into the atmosphere in low-wind conditions, and with it more available moisture for convection, the fuel for the hydrological cycle~~) in the vertical turbulence scheme of ICON XPP (see Section 2.1.2 for details). The minimum wind speed limiter ~~is particularly interesting for a resolution study as it is not only known to be~~ U_{min} has been identified as a promising tuning candidate ~~but~~ to address the double-ITCZ precipitation biases in low-wind regimes such as the Warm Pool (Segura et al., 2025). Additionally, it may also be resolution dependent, with generally ~~more vehement winds~~ increasing near-surface wind speeds at increased horizontal resolution (Jeevanjee, 2017; Iles et al., 2020; Paccini et al., 2021; Morris et al., 2024)~~. The surface wind speed limiter is an example for a "minor-looking treatment" where the lower or upper boundaries of physical parameters are restricted. As "minor-looking treatments" can have impacts comparable to the exchange of parameterization schemes , their implementation should receive more attention~~, making it particularly interesting for a resolution sensitivity study.

In the following, we will show that precipitation biases are reduced with increases in resolution ~~and with an increase in the minimum surface wind speed threshold~~(Sec. 3.1) and physically motivated parameter adjustments (Sec. 3.2.1), both in terms of the large-scale precipitation field and a simplified ITCZ metric. Then we discuss the underlying physical mechanisms of this improvement, ~~including additional focus on the~~ identifying potential trade-offs ~~of~~ between the improved precipitation ~~bias for~~ representation and other key quantities~~, which we proceed to retune in coarse resolution. In a last step, the transferability of the gained knowledge with respect to tuning choices to higher resolution is tested~~. We focus in particular on the impacts on the Hadley and Walker circulation (Sec. 3.2.2), global moisture sources (Sec. 3.2.3), moisture transport (Sec. 3.2.4) and the sensitivity of key global metrics to further tuning (Sec. 3.2.5). We also outline why our experiments hint that the actual ~~root cause for~~ origin of the precipitation biases does not reside in the tropics but in the ~~outer and subtropics~~ subtropics (Sec. 3.2.6). For this purpose, we contrast the real world atmospheric representation~~and energy distribution~~, the one simulated by ICON expressing a ~~dITCZ~~ double ITCZ and the one ~~one~~ simulated by ICON with ~~surface wind limiter~~ tuning adjustments. The identified large-scale differences in the three scenarios ~~are summarized at the end of the work. The reader might find it helpful to refer to the schematic found there throughout the text~~will be visualized building up on Fig. 1. In a last step, we test the transferability of the gained knowledge with respect to tuning choices to higher resolution (Sec. 3.3).

2 Methods

2.1 Model simulations

2.1.1 Model setup

~~Simulations are performed with~~ We perform simulations with the atmosphere model of the Icosahedral Nonhydrostatic Weather and Climate Model for Numerical Weather Prediction, ICON-NWP (Zängl et al., 2015; Prill et al., 2023), in the ~~eXtendedPrediction~~ eXtended Prediction and Projection, XPP-configuration [1] - previously: Seamless configuration (Früh et al., 2022; Niemeier et al., 2023; Müller et al., 2025b). The setup of ICON XPP allows users to conduct weather and climate studies within one consistent framework (Müller et al., 2025a). ICON XPP uses ~~the parametrizations for radiation ecRad~~ parameterizations for radiation (Hogan and Bozzo, 2018), cloud microphysics (Seifert, 2008), ~~turbulent transfer (TKE,)~~vertical diffusion (Mauritsen et al., 2007), convection (Tiedtke, 1989; Bechtold et al., 2008), ~~sub-grid~~ subgrid scale orographic drag (Lott and Miller, 1997)

---

[1] ~~Formerly: Seamless configuration~~

and non-orographic gravity wave drag (Orr et al., 2010)~~together with the JSBACH land model~~. The atmosphere is coupled to the land model JSBACH (Reick et al., 2021).

~~Simulations are carried out in~~ The experiments cover a hierarchy of four horizontal resolutions: ~~R2B4,~~ 160 km ~~; R2B5~~(R2B4), 80 km ~~; R2B6~~(R2B5), 40 km (R2B6), and ~~R2B9,~~ 5 km ~~. This covers~~ (R2B9). This includes the horizontal resolution range of conventional CMIP-type models (160 km) up to the resolution of ~~deep-convection resolving~~ deep-convection-permitting models (5 km). ~~The 80 km and 40 km serve as some additional intermediate resolution steps to test for the impact of i.e. improved orographic representation.~~ For all resolutions, 150 vertical levels up to a model top of 75 km are employed with a constant layer thickness of 300 m from a height of 8.4 km to 19 km~~to fully capture~~. The prescribed constant layer thickness ensures that the altitude range of deep convection is fully captured, even in the inner tropics (Schmidt et al., 2023). ~~For the~~ Two configurations are run at 5 km~~simulations~~. The first configuration relies on the full suite of parameterizations. In the second configuration, the parameterization for ~~sub-grid~~ subgrid non-orographic gravity waves, mid-level and deep convection are disabled~~following the ICON sapphire protocol , however~~. We will refer to this setup as the rParam simulation. In contrast to Hohenegger et al. (2022), the orographic gravity wave drag and shallow-convective parameterization are kept ~~, as in the general numerical weather forecasting protocol~~at all resolutions, as underlying processes are not sufficiently resolved.

2.1.2 ~~Experiments~~

~~For all coarser horizontal resolutions, control simulations – CTL-R2B4, CTL-R2B5 and CTL-R2B6 – are run for six years using~~ In all experiments, we use prescribed 6-hourly climatological sea ice and ~~sea surface temperature fields from the~~ SST fields interpolated from the monthly climatological values of the CMIP6 Forcing Datasets (input4MIPs, 1978-2020) as boundary conditions (Durack and Taylor, 2018). ~~The usage of prescribed, climatological SSTs reduces~~ Prescribed climatological SSTs reduce the impact of interannual variability, such as the influence of ~~ENSO-events on the precipitation. Branching off at the fourth year of these simulations , two-year-long sensitivity studies (perturbed, from here on PTB) are performed in R2B6, varying the minimum surface~~ ENSO events on precipitation. In addition, they separate the effect of model biases in the SST representation and atmospheric processes. The simulations are initialized with data from the European Centre for Medium-Range Weather Forecasts ERA5 reanalysis (Hersbach et al., 2020) for January 1, 2004.

2.1.2 Experiments

Default and U_{min} adapted ICON

U_{min}, the near-surface wind speed limiter, has been suggested as a potential lever for precipitation biases over the Warm Pool region in the ICON sapphire model setup (Segura et al., 2025). In our study, we investigate potential consequences of using this limiter for the global circulation and climate in a resolution hierarchy of the ICON XPP setup.

The near-surface wind speed limiter ~~,~~ U_{min} ~~, presented to the turbulence scheme (Table 1). Specifically, this limiter is set as the squared velocity input $U^2_{total} = U^2_{min}$ for the wind shear term of the~~ acts within the bulk flux formulation in the turbulence parameterization. In this framework, evaporation E is tied to wind speed U at the lowest atmospheric level via the bulk flux formula for evaporation

$$E = \rho_a C_E U (q_s - q_a), \tag{1}$$

where ρ_a is the atmospheric density, q_s surface specific humidity, q_a near-surface ~~moist Richardson number if the squared horizontal velocities with gustiness correction meets the criterion $U^2_{total} < U^2_{min}$. This means that surface fluxes are determined in dependence~~ atmospheric specific humidity, and the bulk transfer coefficient for latent heat C_E , which is inversely proportional to the Richardson number. The bulk flux formulation shows that the latent heat flux is directly proportional to the near-surface wind speed. The fix suggested by Segura et al. (2025) does not change U directly, but adapts a hard-coded lower limit for the near-surface wind speeds. In ICON XPP's turbulence parameterization, the surface wind U used for the computation of the Richardson number has a lower prescribed threshold U_{min} with $U = MAX(U_{min}, U)$. This lower limiter is used to account for the influence of subgrid-scale turbulence with the goal of increasing the turbulent fluxes in low-wind regimes. Increasing the default value of U_{min} ~~in cases where the actual grid-scale wind speed is less than U_{min}. This method has been used to account for~~ from 1 m s^{-1} decreases the Richardson number in low-wind regimes, e.g., in the ~~influence of sub-grid-scale turbulence~~Warm Pool, and leads to increased evaporation. The influence of changes in U_{min} at various resolutions, including in simulations with the full set of parameterizations, has not been tested before. It is important to note that changes in U_{min} can similarly impact turbulent fluxes of sensible heat and momentum in addition to the targeted latent heat flux. Potential consequences of the resulting changes in the momentum budget were not considered in Segura et al. (2025). Concretely, this means that the suggested increase in U_{min} will increase the drag on near-surface winds. It is our aim to investigate whether there are associated negative influences on the circulation next to the positive effect for precipitation over the Warm Pool.

Description of experiment configurations

The simulations presented in this work are summarized in Table 1. We run five control simulations (CTL) in four different horizontal resolutions: 160 km, 80 km, 40 km and 5 km. The simulations are run for six years for all coarser resolutions (160 to 40 km). Due to the very high computation demand, the two 5 km resolution setups - with full parameterization set and reduced parameterization set - are run for three years each instead of six years.

~~For the two settings performing~~ Branching off at the fourth year of the 40-km simulations, two-year-long sensitivity (perturbation) studies are performed (hereafter labeled with PTB). In the perturbation experiments, we vary the minimum surface wind speed limiter, U_{min}, which is presented to the turbulence scheme (Table 1). The two U_{min} settings that perform the best in representing the large-scale annual-mean ~~ITCZ~~precipitation, PTB-5 and PTB-6, with ~~$U_{min} = 5ms^{-1}$~~ U_{min} = 5 m s^{-1} and 6 ~~ms^{-1}, respectively~~m s^{-1}, are chosen for further optimization. First, the wind speed is ~~optimized~~ adapted for land and ocean separately~~(~~. In PTB-5_1 and PTB-6_1, ~~indicating that $U_{min} = 1ms^{-1}$ over land) followed by model retuning (~~U_{min} is set to = 1 m s^{-1} over land to account for the slower near-surface wind speeds. Second, in PTB-5_1t, PTB-6_1t~~) to reestablish the CTL~~ , the model is retuned to reestablish a similar top-of-the-atmosphere (TOA) imbalance to CTL.

~~Due to the exceptionally high computation demand, the CTL-R2B9 is run for three years instead of the six years of the coarser simulations. Subsequent to the coarse scale tuning, the best untuned (~~Only the best performing U_{min} setting, PTB-5_1 ~~) and ~~and the corresponding tuned settings ~~(~~PTB-5_1t~~) are applied to branches off of the CTL-R2B9 simulationfor MAM, the key season for the dITCZ representation, to test the validity of the tuning approach throughout the set of horizontal resolutions~~, are tested in 3-month branch-off runs of the CTL-5 km and CTL-5 km-rParam simulation. For this purpose, MAM is chosen because it is the season with the largest double-ITCZ biases. To allow the model time to equilibrate ~~to~~ with the changed settings~~a one month~~ , a one-month spin-up is used.

As the investigated horizontal resolutions differ by up to a factor of 32, all data sets are remapped for a fair comparison in the subsequent analysis. For this purpose, a 1~~degree~~ ° horizontal resolution is chosen~~, which is near~~ . This resolution is close to the tropical 1.4~~degree~~ ° horizontal resolution of the ~~coarsest simulation, R2B4, with uniform~~ 160 km ~~horizontal grid spacing.~~ simulation.

2.2 ~~Reference: reanalysis~~ Reanalysis and observational data sets

The model output is evaluated against reanalysis and observational data sets. For the radiative fluxes, data from the “Clouds and the Earth’s Radiant Energy System~~, CERES~~" (CERES; Doelling et al. (2013, 2016)), an observational ~~data set~~ dataset for TOA energy fluxes, ~~is used.~~ are used. The precipitation distribution is compared to the observational data sets “Integrated Multi-satellitE Retrievals for GPM~~(IMERG,~~" (IMERG; Huffman et al. (2010)) and “Global Precipitation Climatology Project~~(GPCP,~~ " (GPCP; Huffman (2021)). In addition to these observational data sets, we show radiative fluxes from ~~the fifth generation ECMWF atmospheric reanalysis (~~ERA5, ~~)~~(C3S, 2018; Simmons et al., 2020), noting that these values are not assimilated ~~, which~~ (Dee et al., 2011; Hersbach et al., 2017). This means that the reanalysis product might behave more like a conventional model ~~here~~ for these variables and should only be used ~~as complementing the ground truth~~ to complement the observational data. For latent heat flux, near-surface wind speeds, and near-surface specific humidity q_s, we refer to ERA5 as ~~primary reference~~ a primary reference, as it assimilates station-based humidity measurements (Simpson et al., 2024) and offers a homogeneous data set with values both over land and ocean. Whereas latent heat flux and near-surface wind speeds are direct outputs of ERA5, the values of q_s are ~~derived via~~

$$q_s = \frac{0.622\,p_v}{p_s - 0.378\,p_v}.$$

~~using the vapour pressure p_v in hPa, which is calculated using ERA5 output of 2-m dew point temperature T_D in Celsius and surface pressure p_s in hPa according to the Magnus formula~~

$$p_v = 6.112 \times 5 \exp\left(\frac{17.67\,T_D}{T_D + 243.5\,\mathrm{K}}\right).$$

Table 1. Summary of Experiments: Experiment acronyms, employed resolutions, simulated timeframe, setting for the minimum horizontal wind speed over ocean/land and tuning. The Control control simulation (CTL) run for all resolutions is marked in gray, the best-performing perturbed perturbation experiment (PTB) for the ITCZ large-scale precipitation representation is marked in green. The runs with the reduced set of parameterizations are labeled as rParam. Resolution is given in terms of the ICON grid used and the corresponding horizontal grid spacing.

Experiment	**Resolution**	**Simulated Timeframe**	**Surface Wind Speed Limiter U_{min} (Ocean/Land) / ms^{-1}m s^{-1}**	**Tuned**
PTB-0.5	R2B6, 40 km	2 years	0.5 / 0.5	
CTL	R2B{4,5,6}, 160, 80, 40 km	6 years	1.0 / 1.0	✓
	R2B9, 5 km	3 years	1.0 / 1.0	✓
CTL-rParam	R2B9, 5 km	3 years	1.0 / 1.0	✓
PTB-1.5	R2B6, 40 km	2 years	1.5 / 1.5	
PTB-2	R2B6, 40 km	2 years	2.0 / 2.0	
PTB-4	R2B6, 40 km	2 years	4.0 / 4.0	
PTB-5	R2B6, 40 km	2 years	5.0 / 5.0	
PTB-5_1	R2B6, 40 km	2 years	5.0 / 1.0	
PTB-5_1	R2B9, 5 km	2 MAM	5.0 / 1.0	
PTB-5_1-rParam	R2B9, 5 km	2 MAM	5.0 / 1.0	
PTB-5_1t	R2B6, 40 km	2 years	5.0 / 1.0	✓
	R2B9, 5 km	2 MAM	5.0 / 1.0	✓
PTB-5_1t-rParam	R2B9, 5 km	2 MAM	5.0 / 1.0	✓
PTB-6	R2B6, 40 km	2 years	6.0 / 6.0	
PTB-6_1	R2B6, 40 km	2 years	6.0 / 1.0	
PTB-6_1t	R2B6, 40 km	2 years	6.0 / 1.0	✓

~~In order to assess biases in the~~ computed (details in Appendix A). The ERA5 latent heat flux values ~~a comparison~~ are high biased (Martens et al., 2020; Song et al., 2021). Therefore, we also compare our data to the OAFlux ~~data set~~ dataset (Schneider et al., 2013; National Center for Atmospheric Research Staff, 2022), which integrates satellite retrievals and three atmospheric ~~analyses, is made.~~ reanalysis.

When comparing model data to observational data or ERA5 statistical significance is tested with a two-sided z-test at $\alpha = 0.1$. For the humidity and temperature fields, we correct for autocorrelation via adjustment of the net sample size based on lag-1 autocorrelation values of years 2004-2010 from ERA5 and the 40 km simulations (cf. Trenberth (1984)).

2.3 ITCZ evaluation metrics

To evaluate the ~~bulk~~ large-scale ITCZ features, we use an ~~energetically-motivated framework. Here, precipitation biases can be~~ energetically motivated framework, where precipitation biases are separated into hemispherically symmetric (Adam et al., 2016) and antisymmetric components (Hwang and Frierson, 2013). The symmetric component

$$E_p = \frac{\overline{P}_{2^\circ S-2^\circ N}}{\overline{P}_{20^\circ S-20^\circ N}} - 1 \tag{2}$$

is related to the net energy input near the equator~~where~~. $E_p = 0$ would describe a state ~~where~~ in which the precipitation average $\overline{P}$ between 2° ~~South~~ S and 2° ~~North~~ N is equal to the precipitation average between 20° ~~South~~ S and 20° ~~North~~N. The anti-symmetric component

$$A_p = \cancel{\frac{\overline{P}_{0 N-20^\circ N} - \overline{P}_{0^\circ S-20^\circ S}}{\overline{P}_{20^\circ S-20^\circ N}}} \frac{\overline{P}_{0^\circ N-20^\circ N} - \overline{P}_{0^\circ S-20^\circ S}}{\overline{P}_{20^\circ S-20^\circ N}}, \tag{3}$$

is related to the cross-equatorial energy flux, which is influenced by asymmetries in the net energy input in the high latitudes of the two hemispheres. In both equations $\overline{P}$ is the ~~precipitation averaged over~~ average precipitation in the region constrained by the two latitude boundaries referred to in the respective subscript.

2.4 Residence time in boundary layer based on moisture budget analysis

In order to assess biases in moisture transport, we evaluate the residence time of moisture within the boundary layer. Our analysis is based on a time-mean moisture budget (Peixóto and Oort, 1983; Peixoto and Oort, 1992) linking moisture flux convergence with precipitation and evaporation fluxes as

$$\overline{P} - \overline{E} = -\frac{1}{g}\int_{0}^{p_s} \nabla \cdot \overline{\beta_\rho \mathbf{u} q}\, dp. \tag{4}$$

In this equation $\overline{(\cdot)}$ denotes the annual-mean climatology, $\mathbf{u}$ the horizontal wind vector, q the specific humidity, p is the pressure and g the gravitational constant. β_ρ is a Heaviside function indicating whether values are above or below the surface (cf. Boer (1982)). Based on equation 4, we then estimate the residence time $\tau_{R_{bl}}$ within the boundary layer by splitting the integral into a contribution from the boundary layer up to 850 hPa and the rest of atmosphere and rearranging:

$$\frac{1}{\tau_{R_{bl}}} = \left| \frac{-\frac{1}{g}\int_{850\,hPa}^{p_s} \nabla \cdot \overline{\beta_\rho \mathbf{u} q}\, dp}{\frac{1}{g}\int_{850\,hPa}^{p_s} \overline{q}\, dp} \right| = \left| \frac{\overline{P} - \overline{E} + \frac{1}{g}\int_{0}^{850\,hPa} \nabla \cdot \overline{\beta_\rho \mathbf{u} q}\, dp}{\frac{1}{g}\int_{850\,hPa}^{p_s} \overline{q}\, dp} \right|. \tag{5}$$

Dividing by the integrated moisture within the boundary layer helps control for the dependence of boundary-layer moisture flux on boundary-layer moisture.

2.5 Circulation analysis

We calculate the velocity potential χ at 200 hPa to assess the Walker and Hadley circulation strength following the approach by Tanaka et al. (2004) and Lu et al. (2007) (see Appendix B for derivation details). χ_{max}, the maximum of the zonal-mean velocity potential at 200 hPa within the 30 °latitude band is used as a proxy for the Hadley circulation strength. As χ can only be determined with a constant offset due to the inverse Laplacian, we choose this constant so that the global mean of χ is zero for consistency between the individual experiments. The Walker circulation is the zonally anomalous part of the circulation. Here, we employ χ^*_{max}, the maximum deviation of the annual mean χ in the 10 °latitude band from its zonal mean, as a Walker circulation metric.

3 Results

~~Consistent large-scale precipitation biases across horizontal resolutions~~

3.1 Consistent large-scale precipitation biases across horizontal resolutions

~~To address research question 1, we test if the increase in horizontal resolution and discard of parametrizations reduces the dITCZ bias and investigate where the model resolution has an impact on the model biases. Our analysis of~~ To investigate the ~~yearly-averaged~~ influence of horizontal resolution on the double-ITCZ bias, we focus on CTL experiments with horizontal grid resolutions of 5 to 160 km employing all parameterizations. The two-year mean precipitation shows qualitatively similar biases compared to IMERG ~~data~~ in all four resolutions of ICON (Fig. 2). Quantitatively, there is a consistent improvement in the global root mean square error (RMSE) with respect to IMERG from 1.55 mm day^{-1} (~~R2B4,~~ 160 km) to 1.27 mm day^{-1} (~~R2B9,~~ 5 km)[1]~~. Areas of consistent improvement include coastal regions, e.g., in the ITCZ on either side of South America, and over tropical land, where benefits could partially arise from the improved representation of topographic features. This is particularly true for some of the islands in the Western Pacific Warm Pool, which show a considerable decrease in the dry precipitation bias in the 5 km simulations.~~

hClimatological IMERG precipitation distribution from 2004 to 2010 and two-year mean precipitation bias with respect to IMERG for R2B4 (160 km), R2B5 (80 km), R2B6 (40 km) and R2B9 (5 km) setups. Contours show the IMERG climatology. The corresponding global RMSE in precipitation is stated beneath the panel for each resolution experiment. The global RMSE and mean error in near-surface specific humidity calculated with respect to values derived from ERA5 reanalysis is depicted in the inlays.

~~On the~~ . The large-scale ~~however, all resolutions show the same regions of precipitation biases~~patterns of precipitation bias persist with increasing resolution, but decrease in amplitude. Especially apparent in the tropics ~~are the dITCZ~~ is the double-ITCZ feature over the Pacific and Atlantic, as well as the dry bias over the Maritime Continent~~East Asia, the prominent tropical convective region. The dry bias in the West Pacific and wet biases in the East Pacific hint that the westward transport~~

---

[1] ~~Fig. ?? depicts the significance threshold for a two sided z-test at α=0.1. All major tropical deviations are significant and not marked for better visualization in Fig. 2.~~

~~of boundary layer moisture within the zonally anomalous Walker Circulation is too weak.~~ . Areas of consistent improvement include coastal regions, for example, in the ITCZ on either side of South America, or surrounding the Maritime Continent.

The tropical dry bias over the Warm Pool is tied to a lack of near-surface specific humidity throughout the entire tropics (average global ~~scores~~ values in inlays of Fig. 2; spatial distribution in Appendix Fig. C1). The lack of near-surface specific humidity ~~impacts the vertical moisture distribution and inhibits~~ affects the build-up of larger deep convective systems in the inner tropics and with it the vertical moisture distribution (Fig. 3.1). Consistent for all resolutions, the regions between 20~~°~~° S and 20~~°~~° N are too dry below 1 km in altitude~~. In the 80 km and 5 km simulations, the dry region extends to even higher latitudes in the North~~, although a clear improvement with increasing horizontal resolution is apparent. The lack of ~~boundary-layer moisture in the inner tropics is reflected in the innermost tropical free troposphere~~near-surface moisture helps to explain the lack of precipitation in convective areas close to the equator. In contrast to the inner tropics, the areas between 15~~°~~° to 40~~° North resp. South~~° latitude exhibit a moist bias above 1 km in height, peaking at around 20~~degrees~~° N and S at a height of 2 km. The vertical structure of humidity biases indicates too strong vertical moisture flux out of the boundary layer. The drying of the boundary layer reduces the amount of moisture transported into the inner tropics by the trade winds (Figure 1b). We will demonstrate this mechanism in more detail in Section 3.2.

The consequences of the biases in the specific humidity distribution are also apparent in the ~~zonal mean~~ zonal-mean temperature biases (Fig. 4, cf. Fig~~3.1~~. 3.1 and Appendix Fig. C1). Across the resolutions~~a similar picture persists:~~, a near-surface warm bias and a cold bias in the ~~free troposphere. An exception is the region around 20-40° N, where the near-surface warm bias extends upwards to higher atmospheric layers.~~ tropical free troposphere persist. The near-surface warm bias is most likely caused by the dry bias in the ~~near surface layer~~near-surface layer, which ties the atmosphere closer to a dry adiabatic lapse rate~~which~~. This leads to a warming of the near-surface atmosphere ~~and cooling of the free troposphere aloft. The other findings are consistent with Fig. 2 and Fig. 3.1: The cold bias in the tropical free troposphere is consistent with the reduced deep convection over the Warm Pool. The missing latent heating in the free troposphere leads to a cooler atmosphere or in other words the near-surface dry bias will cause the convection to tie the temperature profile nearer to a~~ as descending air masses heat up more easily. The free troposphere aloft cools: deep convective systems carry less moisture, this reduces latent heat release and ties the temperatures to the steeper dry adiabat. As temperatures in the tropics are quite homogeneous, as explained by the Weak Temperature Gradient theory (Charney, 1963; Held and Hoskins, 1985; Bretherton and Smolarkiewicz, 1989), this bias propagates through the tropical region. The ~~band of warm air~~ warm air band at 20-40° N ~~collocates~~ coincides with the region influenced by the local topography of the ~~Himalaya. Winds following the terrain are directed upwards, advecting tracers and heat . The general free tropospheric temperature bias improves with increasing resolution up to 40 km deteriorating again at 5 km. As the same tuning was used for 40 km and 5 km, this break in bias trend is most likely caused by the discard of the deep convective parametrizations. As simulations with convective parametrizations are know to create a more stable atmospheric temperature profile than their counterparts without convective paraemtrizations , the relatively cooler free troposphere in R2B9 is an expected finding.~~ Himalayas, where the too warm surface air is advected upwards (Pan et al., 2016).

Summarizing~~the findings to the first research question~~, we found that increased resolution ~~and discard of parametrizations~~ alone does not resolve the ~~dITCZ~~ double-ITCZ bias up to a resolution of 5 km. ~~Although improvements can be found in the precipitation pattern, especially in orographically complex regions, similar large-scale biases persist. From these biases~~From the biases, we gain a first ~~mechanistic~~ understanding of the underlying problem: It appears that the negative bias in near-surface specific humidity is one of the causes of the precipitation bias. ~~An increase~~ A negative bias in near-surface moisture ~~would enhance~~ inhibits deep convection in the Warm Pool and ~~strengthen the Walker Circulation. A stronger Walker Circulation would increase~~ weakens the Walker circulation. A too-weak Walker circulation reduces moisture transport from the East Pacific to the West Pacific and further ~~amplify~~ weakens the Walker circulation~~through a feedback loop. Additionally, the deep convection would lead to a warming of~~ . Furthermore, too-weak deep convection leads to a cold bias in the free troposphere, which ~~would increase~~ reduces the temperature inversion ~~in remote regions , including~~ also in distant regions such as the Eastern Pacific, ~~which potentially would lead~~ potentially leading to an additional ~~feedback reinforcing the strengthened circulation , by enhancing~~ positive feedback on the circulation by reducing the cloud cover in the subsidence regions. ~~The differences between observations and ICON results~~ These resolution-independent ICON CTL simulation biases are conceptually summarized in ~~the schematic at the end of the text.~~

Figure 1b. In the following, we will explore an option to counteract against the biases found in ICON by increasing the near-surface moisture and use the resulting perturbation simulations as a test of the mechanistic understanding that we have discussed so far.

3.2 Sensitivity of large-scale precipitation biases to the surface wind threshold in the turbulence scheme

~~With the understanding of the common biases and their potential role in the ITCZ formation, we now focus on the second research question of how to adjust the parameters to counterbalance the found issues in the atmospheric representation. A potential lever is~~ In this section, we investigate the efficacy of a parameter adjustment in addressing the double-ITCZ bias across resolutions in ICON. We test the U_{min} parameter adjustments (Sec. 2.1.2) to address the near-surface ~~humidity~~ dry bias over the Warm Pool region ~~. This would interrupt the vicious~~ with the goal of interrupting the circle of biases outlined in the previous paragraph. ~~Here, the Bulk Flux Formula~~

~~$E=\rho_a C_E U(q_s-q_a)$~~

~~which ties the evaporation E to wind speed U, near-surface specific humidity q_s, atmospheric specific humidity q_a, atmospheric density ρ_a and a proportionally constant C_E, suggest~~ With an increase in ~~horizontal wind speed low-limiter,~~ U_{min}, ~~as a potential lever to address the dry bias over~~ we aim to increase evaporation and near-surface specific humidity. We expect that the increase in near-surface specific humidity will improve the Warm Pool ~~and the related dITCZ biases, because it would increase the U used to compute the near-surface Richardson number and increase surface fluxes in low-wind regimes, e.g. , in the Warm Pool.~~ precipitation and the double-ITCZ feature, through the mechanisms shown in Fig. 1.

3.2.1 The choice of surface wind threshold

~~In a sensitivity study, performed with~~ We use the 40 km resolution configuration ~~, we therefore vary~~ to test the effects of varying the U_{min} ~~in the turbulence scheme to evaluate if it improves the dITCZ bias and the dry bias in the Warm Pool region.~~ threshold in the turbulence scheme. As the mean ~~near-surface-wind~~ near-surface wind speed in the tropics is lower than in the extratropics~~(Fig. 6)~~, increases in U_{min} will have a stronger effect in the tropical region. Starting from the default 1 m s^{-1} setting in the CTL simulation, we change U_{min} to the values of $\{0.5, 1.5, 2, 4, 5, 6\}$ m s^{-1}.

hTwo-year mean large-scale precipitation bias with respect to IMERG 2004-2010 for different settings of the surface wind in R2B6 (40 km) : PTB-0.5, PTB-4, PTB-5, PTB-5_1, PTB-5_1t, PTB-6, PTB-6_1 and PTB-6_1t. Contours show the IMERG climatology. The corresponding global precipitation RMSE is stated beneath the panel for each sensitivity experiment. The global RMSE and mean error in near-surface specific humidity calculated with respect to values derived from ERA5 reanalysis is depicted in the inlays. The resulting two-year mean precipitation biases against IMERG are shown in the first two rows of Fig. 5. Indeed~~the RMSE, both in~~ , RMSEs in both precipitation and near-surface specific humidity ~~, decreases with increasing threshold in surface wind speed up to a~~ decrease with an increase in U_{min} up to 5 m ~~-~~s^{-1} (PTB-5). Going beyond this value increases the RMSE in precipitation again and a positive precipitation bias develops over the Warm Pool ~~(~~in PTB-6~~). Although~~ .

Despite the decrease in the large-scale precipitation bias, ~~i.e., the dry bias over the Warm Pool and the spurious precipitation band in the South Eastern Pacific disappears,~~ precipitation biases over land remain or even worsen. Most apparent is the persistent dry bias over the ~~topographically more complex~~ islands in the Warm Pool region, but also ~~a deterioration of the precipitation fields~~ an increase of the bias over South America and Africa, ~~which develop an increasing dry bias as~~ with increasing U_{min} ~~is increased. We select PTB-5 and PTB-6 as promising candidates for further optimization.~~

~~Observational data suggests~~ (Fig. 5a-d). Observational data show an average wind speed of below 2.5 m s^{-1} at the surface over land, whereas the lower surface roughness over ~~ocean allows for~~ the ocean allows higher wind speeds ~~than over land,~~ with values of 6-7 m s^{-1} (~~cf. Fig. ??~~Fig. 6). High values of U_{min} would therefore cut off more of the velocity distribution over land, leading to ~~a problematic lack of sensitivity of land evaporation to wind speed variations, as well as potentially too large surface drag.~~ exaggerated evaporation over land and potentially drying of the soil. In the next experiments, we therefore distinguish between ocean and land when setting U_{min}, going back to the CTL setting of 1 m s^{-1} for land in PTB-5_1 and PTB-6_1. This ~~more realistic depiction of the surface wind speeds~~ change reverses the increasing dry bias over South America and improves the RMSE precipitation score even further ~~, with PTB-5_1 still outperforming PTB-6_1 (cf.~~ (Fig. 5 ~~(e) and (f))~~e, f).

~~Although the precipitation distribution improves with the changes in~~ In a next step we address the concerns that the increased U_{min}, ~~there are some concerns that it might detrimentally~~ might adversely affect the velocity distribution ~~as already mentioned above. The physical reasoning behind this is that~~ by increasing the surface drag coefficient on the near-surface velocities and correspondingly slowing down the circulation. A comparison of the probability density function of monthly mean surface wind speeds in CTL, PTB-5 and PTB-5_1 with ERA5 in Fig. 6 summarizes how the changes in U_{min} ~~leads to an increase in the~~

~~wind shear term used for the calculation of the Richardson number reducing its magnitude. The smaller Richardson number leads to a less stable atmosphere, enhanced mixing and consequently to an increase of the surface drag coefficient acting on the near surface velocities.~~ feed back on the wind distribution in the tropics. Compared to ERA5, CTL exhibits a skew to smaller surface wind speeds, both over ocean and land. Against expectations, the skew to smaller near-surface wind speeds over ocean is reduced instead of deteriorated via adjustment of U_{min} over the ocean in PTB-5 and PTB-5_1 (Fig. 6b). For the values over land (Fig. 6c), which are mainly in the velocity bins from $0\,\mathrm{m\,s^{-1}}$ to $2.5\,\mathrm{m\,s^{-1}}$, the main velocity peak remains essentially unchanged in location across all ICON simulations, although the probability of strong winds is reduced in PTB-5 relative to CTL.

In the following subsections, we will investigate the impacts of U_{min} changes on the global climate system through the mechanism described at the end of Section 3.1 and depicted in Figure 1. Specifically, we will analyze the impact on the global circulation in Section 3.2.2, explaining why the tropical circulation shows the unexpected strengthening. Section 3.2.3 explores how U_{min} leads to an unintended shift in origin of the inner tropical moisture. In Section 3.2.4, we will demonstrate that ICON exhibits an exaggerated moisture transport out of the boundary layer, which can lead to the deficit in near-surface moisture in the inner tropics. We discuss why this exaggerated vertical moisture transport necessitates high-biased evaporation (i.e. through increased U_{min}) to maintain the global circulation. In Section 3.2.5, we discuss the the global impacts of the U_{min} changes and also how they change with retuning. Section 3.2.6 summarizes the impacts of U_{min} changes on the global dynamics and underlying mechanisms.

3.2.2 The impact of the surface wind threshold: Hadley and Walker circulation

An inspection of the spatially resolved ~~wind fields~~ near-surface wind fields and velocity potential of CTL, PTB-5 ~~,~~ and PTB-5_1 ~~, PTB-6 and PTB-6_1~~ compared to ERA5 in Fig. ~~6 however demonstrates that~~ 7 gives more nuanced insights into the impact of ~~changes in the~~ U_{min} ~~is more complicated. As already seen in the precipitation distribution, the mean impact over land and ocean even goes in opposite directions~~changes on the atmospheric circulation. The choice of ~~unphysical~~ globally high U_{min} ~~values~~ in PTB-5 ~~and PTB-6 leads to an~~ (Fig. 6, Fig. 7e) leads to the expected overall reduction in wind speeds ~~over landas U_{min} impacts the momentum fluxes by artificially increasing the surface drag as outlined above. This~~ on land. Over land, this reduction in overall wind speed ~~above land~~ compared to CTL is reverted when separate U_{min} values are chosen for land and ocean ~~(~~in PTB-5_1 ~~, PTB-6_1, PTB-5_1t, PTB-6_1t). In contrast to the surface wind speeds over land~~ (Fig. ~~6), the surface wind speeds over ocean show a more varied picture. Wind speeds increase in the inner tropics and the Walker Circulation strength, which is too weak in CTL, increases in all perturbation experiments. The perturbation experiments also show improvements in the Northern Hemisphere Trades. Here, the increased moisture supply fueling deep convection and with it the Walker Circulation strength seems to outweigh the increase in surface wind drag. However, other regions where circulations do not depend so much on the additional moisture supply show the expected circulation slow down. For example~~7g). Over ocean, a general slowdown of the Trades in the Southern Hemisphere, e.g., off the West Coast of ~~South-America~~ South America, can be noted in all PTB experiments (Fig. 7e,g). This not only impacts ~~the~~ moisture transport within ~~in~~ the Trades ranging from 30° to the inner tropics, but may also interfere with the wind-evaporation-SST feedback and related teleconnections. The inner tropics are an exception to the general slow-down of the circulation, which would be expected considering the increase in surface drag coefficient. In the next step, we will therefore investigate if the increased moisture supply fuels deep convection leading to an increased Walker circulation strength. This increased Walker circulation strength can then outweigh the influence of increased surface drag.

h(a) ERA5 multi-year average near surface wind speeds for the years 2004-2010. (b-h) Two-year mean large-scale near-surface wind speed bias with respect to ERA5 for CTL and different settings of the near-surface wind speed limiter, U_{min}, in R2B6 (40 km) : PTB-5, PTB-5_1, PTB-5_1t, PTB-6, PTB-6_1 and PTB-6_1t. Arrows visualizing the near-surface wind speed for ERA5 are superimposed on the field change to visualize the general circulation (b-h). The root mean square error and mean error with respect to ERA5 are listed in the bottom right corner for the difference plots (b-h).

~~A comparison of the probability density function of monthly mean surface wind speeds in CTL, PTB-5, PTB-5_1, PTB-6 and PTB-6_1 with~~ Indeed, changes in the velocity potential at 200 hPa confirm changes in the Walker circulation (Fig. 7 b, d, f, h and Tab. 2). In the ERA5 ~~in Fig. ?? over (a) the entire area between 10° S to 10° N, (b) sea-only and (c) land-only values summarizes how the changes in U_{min} feed back on the wind distribution (Fig. ??). Compared to ERA5, CTL exhibits a skew to smaller surface wind speeds which is visible in the wind speed distribution for all selected areas. This mainly reflects the weak Walker Circulation strength in the inner tropics. The skew to smaller~~ reanalysis (Fig. 7 b), the velocity potential field shows a peak in divergence over the Warm Pool and convergence near the coast of South America. For the CTL configuration, the Walker circulation strength is only 80 % of its strength in ERA5 (Fig. 7 c, Table 2). This is in line with the reduced divergence both over the Warm Pool and South America, the locations of rising branches of the Walker circulation. As already suspected from the near-surface ~~wind speeds can be corrected via adjustment of U_{min} in the sea-only area, as seen by improvements in PTB-5, PTB-5_1, PTB-6 and PTB-6~~wind plots, the U_{min} changes improve upon the Walker circulation strength, such that it exhibits the same strength as in ERA5. This is also apparent when comparing Fig. 7 d and f,h where the positive bias of CTL is reduced over the maritime continent. The reduced divergence over the Warm Pool area in CTL is almost entirely counterbalanced at the cost of an increased bias over South America, which shows a decreased divergence. In PTB5_1~~(b). For the values over land (c), which are mainly in the velocity bins from 0 m s^{-1} to 2.5 m s^{-1}~~, the ~~main velocity peak remains essentially unchanged in location across all ICON simulations. However, for the land corrected sensitivity tests PTB-5_1 and PTB-6~~increased convergence over South America decreases again compared to PTB5, further reducing the velocity potential bias (Fig. 7f, h).

The Hadley circulation is generally too weak in all experiments (Table 2). In CTL, the Hadley circulation strength is 70% of its strength in ERA5. In PTB5 and PTB5_1 ~~as well as CTL which also has a U_{min} of 1 m s^{-1}, an increase in the frequency of velocities nearer to 2.5 m s^{-1} wind speed is seen compared to PTB-5 and PTB-6. This feedback of U_{min} on the actual simulated velocity distribution over ocean is in accordance with the starting hypothesis stated above: It is most likely tied to the improved representation of the moisture distribution which wins out over the increases in the drag on the near surface winds. As~~

~~the Warm Pool is now supplied with the required moisture to fuel the deep convection, the Walker circulation is strengthened, the free troposphere is warmed and~~ it drops to 60%. The differing response of the circulation in the ~~corresponding temperature anomaly is propagated through the entire tropics in accordance with the weak temperature gradient theory. Warming aloft increases the inversion over the East Pacific, which could potentially further increase the wind speeds by promoting low cloud formation in the East Pacific and feeding back on the Walker Circulation strength. As seen however in 6, the increased drag on the near-surface wind speeds will reduce~~ innermost tropics and subtropical latitudes can be explained by the increased role of moisture in the inner tropics. More available near-surface ~~wind speeds in higher latitudes - even within the tropics - as the feedback of the~~ moisture leads to increased deep convection ~~on the Walker Circulation and corresponding~~ strengthening the Walker circulation and outweighing the increased drag on the near-surface ~~wind speed increase is confined to the inner tropics~~winds. In the higher latitudes this effect is less important, leading to the slow-down of the Trades and the Hadley circulation.

Table 2. Walker and Hadley circulation strengths for ERA5 as well as CTL, PTB-5 and PTB-5_1. Indices are calculated following the approach by Tanaka et al. (2004) as described in Section **??**

Experiment	**Walker circulation Strength** $\chi*_{max}$ / 10^7 m^2 s^{-1}	**Hadley circulation Strength** χ_{max} / 10^6 m^2 s^{-1}
ERA5	1.16	3.23
CTL	0.94	2.17
PTB-5	1.27	1.98
PTB-5_1	1.22	1.98

3.2.3 The impact of the surface wind threshold: Moisture sources

The changes in the spatial wind speed patterns (Fig. ~~6~~7) have demonstrated that U_{min} has the potential to substantially impact the general atmospheric circulation. It increases the Walker ~~Circulation strength~~circulation strength, but leads to a reduction of the ~~Southern Hemispheric Trade Winds, which~~ Hadley circulation strength, especially noticeable in the region of the Southern Hemisphere trade winds. The trade winds transport a substantial amount of moisture into the inner tropics. ~~The~~ Therefore, the change in U_{min} ~~therefore~~ comes at the risk of changing the weighting of the ~~inner tropical versus outer and~~ inner-tropical versus the subtropical moisture sources. The analysis of the latent heat flux ~~changes~~ biases of CTL, PTB-5 ~~,~~ and PTB-5_1 ~~, PTB-6 and PTB-6_1~~ with respect to ERA5 and OAFlux can give some indication of potential changes in the moisture sources (~~cf. Fig. ??). We additionally show latent heat fluxes from the OAFlux data set which specifically focuses on surface fluxes and integrates satellite and buoy measurements as the latent heat flux is not assimilated in ERA5~~Fig. 8). In the bias plots, a positive evaporation bias with too much moisture release to the atmosphere is visualized in blue, whereas an insufficient evaporation is visualized in red. ~~It is apparent~~ When interpreting these biases, it is important to keep in mind that the latent heat flux ~~by~~ in ERA5 is ~~larger than by~~ high biased (cf. Martens et al. (2020); Song et al. (2021)) and larger than in OAFlux (Fig. ~~?? (a)-(d)).~~ 8 a, b). The biases against ERA5 will therefore tend to have a stronger bias towards more negative values. For consistency with the other plots with the other plots we are using ERA5 as reference, but also add in OAFlux.

CTL shows too little latent heat flux in the region of the ITCZ in the Pacific as well as in the Indian Ocean with respect to ERA5 (Fig. ~~?? (c)).~~ 8 c), whereas values compared to OAFlux almost perfectly capture the zonal-mean climatology. ~~With respect to OAFlux (Fig. ?? (d)), which shows lower latent heat fluxes than ERA5 (Fig. ?? (b)), a general overestimation of latent heat fluxes is already present in CTL, with only a negligible underestimation near the Warm Pool and at the ITCZ.~~ With the increase in U_{min} (Fig. ~~??(e),(f)~~8e-h), the low ~~biases~~ bias in the Warm Pool region ~~are reverted to~~ is reverted to a positive latent heat flux ~~biases~~bias, leading to ~~an excess~~ a too strong latent heat flux in the tropical region, even compared to the already high values simulated by ERA5. ~~In the Eastern Pacific, the negative evaporation bias in the northern ITCZ region is reduced~~Although the spatial contrast in evaporation reduces, negative evaporation biases emerge in the trade wind regions at the coasts of Central- and South-America, key source regions for moisture transported into the tropical Pacific. These reductions are obscured in the zonal mean, because subtropical regions with climatologically lower wind speeds, such as the region South-East of Australia, develop positive evaporation biases. However, ~~especially in the Central Pacific, a more pronounced positive bias develops as more moisture evaporates with the higher near surface wind speeds. This change occurs in a region where OAFlux and ERA5 show relative consistency. Additionally, negative evaporation biases emerges in the Trade Wind regions at the coasts of Middle-~~ as this is a region of relatively little moisture-flux convergence, the moisture lingers in the region of evaporation. All in all, these findings indicate a reduction of the subtropical moisture contribution to moisture in the Pacific inner tropics.

3.2.4 The impact of the surface wind threshold: Moisture transport

Next we investigate the potential role of vertical moisture transport out of the boundary layer at latitudes between 20° and ~~South-America, indicating a reduction of the outer- and subtropical moisture source. All in all, there is a shift in the location of evaporation from the outer- and subtropics to~~ 40° in reducing moisture transport by the trade winds into the inner tropics. This exaggerated vertical moisture transport out of the boundary layer could lead to the negative near-surface humidity bias in the inner tropics (cf. Fig. 3.1). If this is the case, then strong evaporation in the ~~tropics in the perturbation experiments compared to CTL, leading to a reduction in spatial contrasts in evaporation biases. However, there is an increase in global-mean latent heat flux leading to too much evaporation overall.~~innermost tropics is necessary to compensate for the lack of moisture transported into the tropics. However, this would also mean that the wind speed limiter fix addresses a downstream consequence and not the primary error in moisture transport.

Figure 9 shows the inverse residence time $\tau_{R_{bl}}$ of specific humidity within the boundary layer up to 850 hPa (Section 2.4). The reference values for ERA5 (Figure 9 a) exhibit shorter $\tau_{R_{bl}}$ (larger $\tau_{R_{bl}}^{-1}$) on land compared to ocean. On a large scale, the $\tau_{R_{bl}}$ values simulated in CTL, PTB-5, and PTB-5_1 are shorter compared to ERA5 (Figure 9d-f), demonstrating a too fast loss of boundary layer moisture to the free troposphere. This transport bias is well aligned with positive specific humidity biases in the free troposphere in the mid latitudes shown in Figure 3.1. The fast loss of boundary layer moisture is most pronounced in the higher latitudes around the poles, but tropical and midlatitude land as well as the trade wind region are also affected. In CTL, the weaker circulation manifests itself in a pronounced bias to longer residence times in the Northern ITCZ band over the Eastern Pacific, which is indicative of too weak moisture-flux divergence. With the U_{min} adaptation, this bias is corrected at the expense of an overall shortening of residence times in the trade wind region.

A quantitative analysis of $\tau_{R_{bl}}$ over the ocean only demonstrates that the probability density function of $\tau_{R_{bl}}$ is biased to shorter residence times without apparent improvements with the U_{min} patch (Figure 9c). The corresponding bias in the zonal distribution of $\tau_{R_{bl}}$ over the ocean compared to ERA5 confirms that shorter residence times dominate over all latitudes in the ICON experiments (Figure 9b). The U_{min} adjustment does not correct the short $\tau_{R_{bl}}$ values in the tropics, where values were already too short. In the region at 10 °N, where CTL exhibited long residence times, it overcompensates the bias. In the subtropics the bias is slightly improved. However, with increasing land masses, especially in the north, the bias increases again, almost doubling in the case of PTB-5_1 at 40 °latitude.

Together, these results illustrate that moisture is exported too quickly out of the boundary layer to the free troposphere in the ICON simulations, which leaves less moisture for transport to the inner tropics. The change in U_{min} does not directly correct for this problem, but combats the consequences by artificially increasing the moisture supply to the boundary layer, specifically in low-wind regimes in the tropics. A more physically motivated correction would be to increase the transport of subtropical moisture into the tropics rather than the subtropical free troposphere. The consequent increase in inner-tropical moisture source would likewise lead to a increase in the Walker circulation. This would naturally increase the near-surface wind speeds and compensate for the missing evaporation in the tropics.

3.2.5 The impact of the surface wind threshold: global variables

As we have seen far-reaching impacts on the general atmospheric circulations when U_{min} is increased, we investigate the impact of the altered U_{min} on ~~other physical key~~ key global parameters in Fig.~~7~~10. The first parameter pair is the asymmetry index A_p and symmetry index E_p of the precipitation distribution. All sensitivity experiments show a positive A_p, consistent with the observational references IMERG and GPCP, indicating that the inter-hemispheric energy imbalance is captured correctly. E_p shows negative values, starting to increase only at a U_{min} of $4\,\mathrm{m\,s^{-1}}$. ~~This value, which reflects~~ The negative E_p for U_{min} limiters smaller than $4\,\mathrm{m\,s^{-1}}$, reflect the large dry bias over the Warm Pool~~,~~. They indicates that the net energy input (NEI) to the atmosphere at the equator is most likely low biased. Since U_{min} preferentially effects evaporation in warm regions where evaporation is climatologically high and regions with low wind speeds, an increase in near-surface wind speed will have a more substantial effect in the inner-tropics~~(cf. Fig. ??)~~, which would positively reflect in the E_p index, as is evident in the simulation scores.

The simulations scores ~~also show how the global latent heat flux increases with increasing U_{min} which is also reflected in an increase in the near-surface specific humidity . A comparison of both values with the corresponding reference from ERA5~~

~~shows that whereas the bias in~~ confirm that the correction in the low biased near-surface ~~specific humidity decreases, the~~ humidity with U_{min} comes at the cost of a high biased global latent heat flux ~~bias increases~~ compared to ERA5 (cf. Fig. ~~??~~ 8 and Fig. C2 for spatial maps). ~~The high bias in the global latent heat flux in combination with the low bias in global near-surface specific humidity point towards an additional underlying problem for which U_{min} only combats the symptoms rather than the root cause.~~

~~Insight into the underlying problem can be inferred from examining the spatial maps of latent heat flux and near-surface specific humidity biases and their changes (Fig. **??** and Fig. C2). The increase in U_{min} leads to a reduction of latent heat flux RMSE as negative biases are reduced in the inner tropics, but it does this at the cost of an increase of the mean latent heat flux high bias as positive biases remain high in the subtropics, which in other words would say that the large bias in spatial patterns is reduced at the cost of a more uniform bias. This indicates that in total there is enough moisture available in the atmosphere through evaporation~~Globally already enough moisture is supplied to the atmosphere in CTL, but there are ~~problems with~~ biases in the moisture distribution ~~through~~ associated with the global circulation. ~~U_{min} seems to compensate for three problems in the moisture transport. First, for a too strong transport out of the boundary layer in the 0-30 latitude band. Second, for a consequently too weak horizontal equatorward near-surface specific humidity transport within the Trades from the outer and tropics, the main source region of inner tropical moisture . Third, for an insufficient upward transport of this moisture in the main deep convective regions by supplying a surplus in moisture. We will revisit this hypothesis in the overall interpretation of the coarse and high-resolution simulations in section 3.3.~~

The improvements of ITCZ bias ~~and near-surface specific humidity~~ comes at the cost of strong biases in the global year-mean net top-of-the-atmosphere (TOA) imbalance which drops by ~~almost 4 W m^{-2} for a U_{min} of 5 m s^{-1} and~~ 5 W m^{-2} ~~respectively~~ for a U_{min} of 6 m s^{-1} (Fig. ~~7~~10). The main contribution to the changes in TOA imbalance arise from upward shortwave radiation which increases substantially as the cloud cover increases. Due to the specified-SST setup~~and the timeframe of the simulations~~, the increased bias in TOA imbalance can only have small ~~effect~~ effects on the surface temperature T_s ~~arising from the~~ as temperature changes at the surfaces are restricted to sea ice and land only. Despite the negative TOA, T_s increases by around 1 K. This can be explained by the increase in free tropospheric moist static energy, as both specific humidity values and atmospheric temperature increase while the lapse rate over land does not change substantially (Zhang and Boos, 2023). The increase in T_s is reflected in the increase in outgoing long wave radiation. The tuning simulations 5-1t and 6-1t ~~(explained in Section 2.1.2)~~ demonstrate that it is possible to readjust the radiative fluxes to expected values without strong deterioration in the improved precipitation distribution.

hTuning scores for all R2B6 (40 km) sensitivity experiments as a function of prescribed minimum surface wind speed. The values for a U_{min} of 1 are the CTL settings and where taken from the respective two years of the CTL simulation. Values for the asymmetric index A_p, symmetry index E_P as well as latent heat flux, near-surface specific humidity q_s, net top-of-the-atmosphere (TOA) imbalance, upwards radiative shortwave flux, outgoing long wave radiation (OLR) and global mean surface temperature T_S are shown. Each point depicts one global year average. For reference the corresponding values from IMERG, GPCP, ERA5 and CERES are depicted.

3.2.6 The impact of the surface wind threshold: Consequences on global dynamics

Within this section, we have answered the first part of the second and a large portion of the third research question group: The precipitation biases in ~~coarse scale~~ coarse-scale 40 km simulations can be addressed by increasing evaporation via an increase in U_{min} in the turbulence scheme. Mechanistically, the increase in U_{min} should lead to an increase in the drag on the surface winds. ~~In~~ However, in the inner tropics~~however~~, the increase in U_{min} also counterbalances the dry bias in the Warm Pool region through ~~its influence on evaporation.~~ increased evaporation. This fuels deep convection and leads to an acceleration of the Walker circulation transporting spurious moisture over the Eastern and Central Pacific into the main convective region. The increase in the Walker ~~Circulation~~ circulation strength counterbalances the increases in drag on the near-surface wind speeds in the inner tropics, leading to an increase in near-surface wind speed over ocean. In the subtropics, which do not benefit from the increase ~~Walker Circulation~~ in Walker circulation strength, the increased drag on the surface winds leads to a reduction in the ~~Trade Wind strength.~~ trade wind strength. U_{min} compensates for three problems in the moisture transport:

1. for too strong vertical transport out of the boundary layer (cf. Fig. 9).
2. for the consequently too weak meridional equatorward near-surface specific humidity transport within the Trades from the subtropics (cf. Tab. 2), the main source region of inner tropical moisture (Schneider et al., 2014).
3. for the resulting dry bias in the tropics and too weak moisture transport by tropical circulations.

By drawing the moisture primarily from the inner tropics without fixing the problem in the vertical transport in the higher latitudes, it however acts more like a "patch" than a real fix. The improved representation of the ITCZ ~~therefore~~ comes at the cost of ~~an~~ a replacement of higher latitude (sub)tropical moisture sources by an increase in the inner-tropical moisture source, a reduction in the ~~Trade Wind strength~~trade wind strength, and an increased ~~global mean~~ global-mean latent heat flux bias (~~cf. Fig.12~~Fig.1c).

3.3 Transferability to higher resolutions

After understanding the sensitivity to U_{min} changes in the coarser ~~R2B6~~ 40 km setup, we proceed to ~~answer the second part of research question 2 and test if~~ investigate whether the corresponding improvements with U_{min} also translate to ~~the higher resolution, R2B9 (~~higher 5 km ~~)~~resolution and additionally whether discarding parameterizations improves the representation of the mean atmospheric state. Due to computational constraints, we ~~concentrate on~~ perform seasonal rather than ~~yearly averages in the precipitation feature, focusing~~ year-long sensitivity tests. We focus on two MAM seasons, as ~~it~~ this is the key season for the ~~dITCZ~~ double-ITCZ bias (e.g., Si et al. (2021); Adam et al. (2018)). A comparison of the precipitation bias for the CTL ~~, PTB5-1 and PTB5-1t simulations in R2B6 and R2B9~~ and PTB5-1 simulations in 40 km, 5 km and 5 km-rParam is shown in Fig. ~~8, demonstrating that biases are also reduced by~~ 11. The 5 km setup with the full suite of parameterizations exhibits a less pronounced double-ITCZ feature in the East Pacific than rParam, its counterpart without gravity wave and deep convective parameterization (Fig. 11b,e; cf. Fig. 11c,f). Additionally, while the 5 km-Param setup reduces the global-mean near-surface specific humidity bias compared to the 40-km setup, the 5 km-rParam setup increases the global-mean near-surface specific humidity bias. However, especially in the MAM average, it becomes apparent that the precipitation dry bias over the Warm Pool is stronger in the parameterized simulations (Fig. 11e; cf. Fig. 11f), with an RMSE comparable to the 40 km setup. This is also true for the dry bias over the islands in the Maritime Continent, which disappears in rParam but is still apparent in the 5 km setup with the full set of parameterizations.

In both 5 km configurations, the seasonal-average double-ITCZ bias is reduced by U_{min} ~~changes in the higher resolution simulations . Within the seasonal comparison, the R2B9 already shows a reduced RMSE compared to R2B6~~changes, and their RMSE in seasonal-average precipitation is less than in the comparable 40 km simulations. It can therefore be expected that ~~R2B9 is~~ the 5 km setups are likely to outperform the coarser resolution simulations ~~also~~ in longer timeframe PTB-5_1 simulations, as was already the case in the CTL simulations (Fig. 2 ~~). Again, it is especially noticeable that the R2B9 does not exhibit the persistent dry bias over the islands over the Maritime continent~~and Fig. 11 a, b, c). The positive precipitation bias appearing in the Indian Ocean with the U_{min} adjustments is not as prominent ~~in higher resolution . Both resolutions show remaining precipitation biases in the Atlantic. However, while the ITCZ precipitation bias over the Atlantic is fused to a single precipitation band with Northward emphasis in R2B9, it is more diffuse in the R2B6 simulations with a more pronounced southern emphasis. The seasonal location of the ITCZ in MAM has a tendency towards the South . In this regard the R2B6 Atlantic bias could improve the A_s index (~~at higher resolution (Fig. 11h, i; cf. Fig. 11~~), whereas the R2B9 Atlantic bias deteriorates it~~g). In contrast to the ~~R2B6 simulations, the mean near-surface specific humidity bias is not fully neutralized in the R2B9 setup, although it is more than halved~~40 km setup, both 5 km setups also show strong improvements in the precipitation biases over the tropical Atlantic.

~~Figure 9 visualizes the changes in the bias of the zonal specific humidity distributionin MAM for R2B6 and R2B9 against ERA5, both for the untuned and tuned PTB-5_1 versions. In R2B6, the dry bias in the inner tropics reverses (from Subfig. (a) to (c) and (e) in Fig. 9), while the bias between~~ Across all simulations, the 40 km and 5 km-Param setups show similar biases in the moisture distribution, but with reduced amplitude at increased resolution (Figure 12). In the CTL simulations, the near-surface dry bias is much more pronounced in 5 km-rParam than in the 40~~t o 20 latitude above 1 to 2~~ km ~~deteriorates. This again hints at the too efficient vertical transport out of the boundary layer into the free troposphere, most likely in regions of shallow convection, and insufficient horizontal moisture transport starting at 30 latitude into the tropics. In R2B9-CTL, the near surface dry bias is far more pronounced than in R2B6-CTL, changing the baseline for the tuning. The~~ and 5 km-Param setups. In all setups, the increase in U_{min} reduces the dry bias and changes the sign of the inner-tropical dry bias up to 3 km~~, greatly reducing it in the levels above. At 20°N, the near surface dry biasimproves without disappearing, whereas it almost disappears at 20°S. The reduced dry bias in the Southern Hemisphere leads to an increase of the moist bias in higher atmospheric levels whereas the situation in the Northern Hemisphere remains approximately unchanged. Overall, with increased U_{min} the specific humidity bias changes to positive everywhere in the lower resolution and biases are reduced in magnitude in the higher resolution~~. In the setups with parameterizations, the U_{min} fix counterbalances the near-surface specific humidity dry bias, while leading to a slight deterioration of the free tropospheric moisture bias at higher latitudes. In the 5 km-rParam setup, the near-surface humidity dry bias can not be entirely counterbalanced by the U_{min} fix, however, the free tropospheric moist bias does not increase as much. The remaining ~~surface bias~~ near-surface bias in PTB-5_1-rParam at 5 km resolution amounts to a ~~percental~~ percentage bias of less than 3 percent~~resp.~~ , 15 percent of the background values in ~~R2B6 and R2B9~~40 km and 5 km. Overall, despite the ~~outlined differences in the~~ differences described between the two resolutions, both ~~R2B6 and R2B9~~ 40 km and 5 km exhibit the same symptoms of a ~~too strong~~ too-strong vertical moisture transport from the boundary layer into the free troposphere between ~~40 t o~~ 20 to 40° latitude, which comes at the cost of reduced near-surface moisture transport into the tropics, and this remains the case in rParam.

The increase in atmospheric specific humidity and deep convection in the inner tropics with modified U_{min} is also visible in the ~~zonal mean~~ zonal-mean temperature biases in Fig.~~10~~13. The tropical free troposphere warms in both resolutions as the convection ties the temperature profile to a different ~~base line~~ base-line moist adiabat with increased moisture supply. In ~~R2B6 the~~ the parameterized setups, the cold bias is overcompensated, resulting in a warm bias~~, whereas the R2B9 resolution shows an overall improvement~~. The 5 km-rParam exhibited a stronger cold bias than the parameterized setups. Here, the cold bias is reduced. A possible reason for the differences in the zonal-mean temperatures could be differences in the entrainment rates into the convective cores in the parameterized and non-parameterized simulations. The more pronounced cold bias in the 5 km-rParam setups suggests that more entrainment takes place in the simulations relying on explicitly described deep convection, resulting in an overall colder tropical free troposphere.

~~The simulation scores are summarized in Fig.11, where the re-tuning was performed~~ Next, we re-tune the 5 km setups with the same parameter adaptations used in ~~R2B6 (~~40 km ~~)~~ to test the transferability of the tuning to higher resolution. ~~In almost all variables, R2B6 and R2B9~~ The simulation scores from this exercise are shown in Fig.14. In many variables, 40 km and 5 km behave similarly, although it is also evident that the ~~R2B9~~ 5 km simulations exhibit a greater spread (i.e., variability) than the coarser ~~R2B6~~ 40 km counterpart for some variables. In A_s all simulations perform well compared to IMERG, although the 5 km-rParam simulations exhibit a small positive deviation. The E_p score is ~~already almost within observational constraints~~ negatively biased in the untuned version and improves for both resolutions with ~~wind surface tuning~~the U_{min} adjustment. The improvement in near-surface specific humidity comes at the cost of an increased bias in latent heat flux~~, again indicating problems in the vertical and horizontal moisture transport. The top-of-the-atmosphere~~. The TOA radiative imbalance shows increased variability in the ~~R2B9~~ 5 km simulations. The main simulation from which the sensitivity experiments were branched off shows maximum jumps in ~~year-mean~~ annual-mean TOA imbalance of 0.4 Wm^{-2}, with no clear ~~trend~~ drift in the three simulated years~~, so there is no indication of a spin-up problem. Instead the resolved convective processes probably play a role in the increased variability, as they will show their signature in both the~~. This suggests that newly resolved processes enhance variability, both in SW up (~~especially~~ suggesting a role for low clouds) and OLR (~~especially~~ suggesting a role for high clouds). The global-mean near-surface temperature T_s is the only parameter in which ~~the two resolutions~~ different setups show opposing trends with adjustment of the U_{min} and tuning: warming for ~~R2B6~~ parameterized setups and cooling for ~~R2B9. For both resolutions~~5 km-rParam. For the 40 km and 5 km-rParam setups, the tuned versions are coming ~~nearer to observational~~

~~values however. As~~ closer to the observational values. The 5 km simulations with parameterizations shows a deterioration in T_s ~~is very closely related to orographic wave drag which again depends on the representation of the topography, resolution differences with otherwise identical tuning can be expected.~~ bias.

Summarizing the main findings in this section, we demonstrated ~~the transferability both of~~

1. that the U_{min} adjustment to counteract the development of the ~~dITCZ as well as the R2B6 tuning to~~ double ITCZ is similarly effective in 5 km simulations as in 40 km simulations and
2. that the 40 km tuning is transferable to the 5 km-Param simulations with sole adjustments of the orographic tuning parameters.

We also showed that the ~~R2B9 simulations . We showed that also~~ humidity and temperature fields change in a similar fashion ~~but different amplitude to~~ to the adjustments of U_{min} ~~adjustments. In addition, we discussed the underlying mechanisms in more detail. Specifically, that the actual root cause of the dITCZ bias is not the dry bias in the Warm Pool, but an insufficient transport of moisture from within the 0-30 latitude band to the inner tropics (cf. Fig. 13). Indications for this are found in Fig. 6, Fig. **??**, Fig. 7 and Fig. 9.~~ at different resolutions.

4 Discussion and Conclusions

In our study, we compared the representation of the precipitation as simulated by ICON over a resolution hierarchy spanning from CMIP-resolution up to km-scale. Although some small-scale improvements, such as a better representation of precipitation over land with more pronounced orography were found, increased resolution and the discard of deep convective and non-orographic gravity wave ~~parametrization~~ parameterization could not resolve persistent large-scale precipitation biases. The large-scale precipitation biases found in our ICON resolution hierarchy are consistent with the ~~dITCZ~~ double-ITCZ bias present through several CMIP generations (Tian et al., 2024). Additionally, we find a too-cold ~~and~~ tropical free troposphere and a too-moist free troposphere ~~, which are especially pronounced in the midlatitudes, although the latter already emerge at around 20° latitude~~in the subtropics. These biases are symptoms of a general misrepresentation of the exchange of energy and moisture between the inner- and outer tropics (Fig. ~~12 (a)~~1 a, cf. Fig. ~~12 (b))~~1 b).

To address the biases, we focused on the parameterizations that remain active at the km-scale, focusing on U_{min} in the ~~turbulence scheme, which~~ bulk flux formulation of the turbulence scheme. It is known that the bulk flux formulation can lead to biased results compared to observations in both very low and very high wind regimes, producing a high bias in latent heat release (Hsu et al., 2022). Additionally, adjusting U_{min} yielded promising results in the Sapphire configuration of the ICON model (Hohenegger et al., 2022; Segura et al., 2025). The usage of increased U_{min} in the bulk flux formula resolved some of the precipitation biases~~; however, we found~~. This improvement came at the cost of a global overestimation of evaporative fluxes. Furthermore, a deterioration of precipitation over the land ~~making~~ made a separate adjustment necessary. This was not seen in Segura et al. (2025) due to their focus on the ~~dITCZ~~ double-ITCZ feature in the Warm Pool region. Furthermore, we showed that the ~~wind surface tuning~~ U_{min} adjustment led to similar changes at the km-scale as in our lower-resolution simulations, indicating that tuning lessons learned at lower resolution can be applied to km-scale simulations. Our analysis also gives new insights into the mechanisms by which U_{min} acts: ~~An increase in the wind speeds~~ By increasing evaporation, it counterbalances the low biases in the near-surface specific humidity in the tropics, enhancing deep convective activity, which increases free tropospheric temperatures and the temperature inversion in subsidence regions.

~~However, further analysis also made some caveats with respect to changes in U_{min} evident. Although U_{min} improves the representation of the mean of the wind speed distribution in the innermost tropics, it introduces biases in its regional and temporal variability seen by the turbulence scheme. The increase in the mean state makes wind extremes to appear less pronounced as part of the low wind speed spectrum is cut off by U_{min}. This concern can be attenuated when considering that the "prescribed" bias in the velocity distribution is only seen by the turbulence scheme. Additionally, have found that the correlation between wind speed and precipitation mainly is not related to mesoscale gustiness but triggered by increases in the mean surface fluxes. Focusing on these very surface fluxes, it is known that the bulk flux formulation can lead to biased results compared to observations both in very low and very high wind regimes, producing a high bias in latent heat release. This behavior is also present in ICON. The uniform increase in U_{min} increases the latent heat flux bias globally, showing only improvements in the originally low-biased Warm Pool region. The increase of latent heat release in the Warm Pool region corrects for the lack in net energy input in the inner-tropical region which is implied by the E_p index. Given the negative impact on the biases in latent heat fluxes, we suggest that a wind speed limiter that accounts for regional differences in wind speed distributions would be a superior solution.~~

The fact that the model can not replicate the observed near-surface wind distribution hints at more overarching problems in the global near-surface moisture advection. The increase in U_{min} speed acts to address the too weak Walker ~~Circulation~~ circulation but does not address the lack of moisture transport from the higher (sub)tropical latitudes starting at 30 °latitude, which is likely the origin of the tropical dry bias (Fig. 12 ~~(c)). If this understanding is correct,~~ c). This also means that the additional supply of near-surface moisture is drawn from the wrong location, i.e. the inner tropics instead of the ~~higher latitude (sub)~~subtropics. Our moisture budget analysis shows an exaggerated vertical moisture transport out of the boundary layer (cf. Fig. 9), which explains the deficit in moisture available for transport into the inner tropics. The study by Lang et al. (2023) ~~who performed trajectory analysis for humidity parcels supports this hypothesis. They could~~ gives further evidence that exaggerated vertical moisture transport out of the boundary layer is related to turbulent transport. They also demonstrate that tropical moisture biases are greatly influenced by insufficient transport from the ~~higher latitude (sub)tropics~~subtropics. In addition, they described the tendency of the TTE turbulence scheme used in this ICON configuration to act similarly to a convection scheme, also in higher atmospheric layers. Huusko et al. (2025) in turn demonstrate that there are no significant changes in the effects of turbulence boundary layer schemes with increasing resolution. Their and our findings combined ~~would~~ can explain the positive moisture bias in the higher layers of the subtropical atmosphere - they are caused by the tendency of the turbulence scheme to transport moisture upwards out of the boundary layer like a convective scheme. This situation may be aggravated if parameterizations such as the deep convective parameterization are discarded prematurely. Another source of the bias might also be the shallow convection; however, as ~~the same bias was~~ similar biases were also encountered in the ICON sapphire configuration without the shallow convection scheme (Segura et al., 2025), a bias in the used turbulence schemes or in the dynamical core is more likely.

In summary, the main findings of this work are:

1. Similar large-scale precipitation biases persist throughout the ICON resolution hierarchy up to km-scale resolution, although improvements ~~in orographically prominent regions~~ over tropical islands in the Warm Pool region appear with increasing resolution and discard of parameterizations.

2. Precipitation biases can be resolved by adapting undiscardable ~~parametrizations~~ parameterizations but only yield an overall improvement of the precipitation fields if ocean and land are treated separately. The direction of regional changes hold over various resolutions. The main driving mechanism is a strengthening of the Walker ~~Circulation~~ circulation by increasing the supply of available moisture for the deep convective regions. However, the U_{min} fix proposed by (Segura et al., 2025) leads to additional drag on near-surface winds in higher latitudes. If the U_{min} limiter has to be used as a patch, it may be advisable to at least restrict it to the bulk flux formula for evaporation and not those for momentum exchange and sensible heat.

3. There are strong indications that ~~this~~ the U_{min} fix is not addressing the underlying core problem. A uniform wind threshold does not account for different regional circulation regimes and will lead to too high evaporation values in regions with low wind speed variations. Especially noticeable is also that the global latent heat flux and the ~~40 to~~ 20° ~~latitude free tropospheric~~ to 40° latitude free-tropospheric moisture bias are increased in the ~~retuned~~ adjusted simulations. This ~~hints~~ demonstrates that there are problems with the source regions and transport of atmospheric moisture. ~~There is some indication that the~~ The fix leads to a replacement of subtropical moisture by moisture originating from the inner tropics~~and~~. Additionally, the increase in drag on the near-surface wind speeds leads to a slow down of the ~~Trades windswhich indicates~~ trade winds, such that the adjustment might compromise the representation of extra-tropical to tropical teleconnections.

4. Results indicate a two-fold faulty representation of the moisture transport (including by ~~parametrizations~~parameterizations) in ICON, and potentially in the many other models with a ~~dITCZ~~ double-ITCZ bias:
   - In the subtropics, the vertical moisture transport out of the boundary layer is too strong, leaving ~~less~~ too little moisture to be transported horizontally within the Trades into the tropics.
   - In the tropics, the lack of moisture reduces deep convective activity, which in turn reduces temperature inversions and slows down the Walker ~~Circulation~~circulation. The reduced zonally anomalous circulations favors the development of a second ITCZ branch as moisture is not transported into the core regions for deep convection.

The differences in moisture and energy export found in the observations, the world simulated in the CTL ICON and the ICON with ~~wind speed adaptations~~ U_{min} adjustments are depicted in Fig.~~12~~1.

The results of this study suggest that a two-fold climate modeling strategy would be greatly beneficial for the community: On the one side the advancement of high-resolution simulations by larger institutions with vast computational resources. On the other side~~the~~ , further development of necessary ~~parametrizations~~ parameterizations and coarse-scale models~~in close collaboration with theoreticians~~. The persistence of large-scale biases ~~found in~~ across our ICON resolution hierarchy shows the potential of learning both from high- and low-resolutions. This approach was also demonstrated in the tuning of the precipitation biases in the NICAM model which specifically addressed and learned from ~~resolution independent~~ resolution-independent biases (Takasuka et al., 2024). In the long term, scale-aware ~~parametrizations, potentially~~ parameterizations or parameterizations with a seamless transition between convective and ~~sub-grid~~ subgrid scale turbulent processes within one unified scheme (~~i.e.~~e.g., Tan et al. (2018)), might build a bridge between the high- and low-resolution modeling strategies.

hConceptual depiction of the main zonal and meridional circulations exchanging moisture and energy between the subtropics and the tropics as a) observed, b) in conventional ICON simulations, and c) in U_{min} adjusted ICON simulations. Observations show that the moisture within the innermost tropics originates from evaporation in tropical and subtropical areas. The moisture is imported into the innermost tropics by the Trade Winds, with small losses to the free troposphere. In the innermost tropics it is then transported to the main convective regions, i.e., the Warm Pool (WP) within the zonally anomalous Walker circulation. Energy is exported to the subtropics within the outward branches of the Hadley circulation. In conventional ICON simulations (b), a large portion of moisture is lost due to too much vertical transport of moisture from the boundary layer to the free troposphere between 0and 30latitude. This leads to a moisture deficit in the tropics, specifically over the WP, reducing deep convection, slowing down the Walker Circulation and leading to spurious additional convective centers over the Eastern Pacific as too little moisture is transported to the WP within the boundary layer. In the wind speed corrected ICON world (c) increased surface wind speed lead to an additional moisture source in the tropics which resolves the dry bias over the WP. However, the adjustments increase the overexpressed free tropospheric moisture bias between 0to 30~~, reduce the Trade Wind strength, lead to a too strong Walker Circulation and most importantly change the balance between innermost-tropical to (sub)-tropical contribution to the tropical moisture content. Green colors indicate high moisture content. Brown colors low moisture content.~~

Code and data availability. The ICON code was released in January 2024 under https://www.icon-model.org/news/news_open_source_release. The ICON XPP code release and source scripts are publicly available and published by (Müller et al., 2025b). The model data and postprocessing scripts needed to replicate the work presented in this paper will be made available upon publication in a zenodo archive. The ERA5 reanalysis data set is available from the climate data store (https://cds.climate.copernicus.eu/). IMERG is provided by NASA under https://gpm.nasa.gov/data/directory. GPCP data sets are maintained by NOAA under https://psl.noaa.gov/data/gridded/data.gpcp.html. CERES data can be obtained from NASA under https://ceres.larc.nasa.gov/data/. The OAFlux data are maintained by NCAR under https://climatedataguide.ucar.edu/climate-data/oaflux-objectively-analyzed-air-sea-fluxes-global-oceans. For postprocessing and data analysis python and CDO were used, the latter can be downloaded under https://code.mpimet.mpg.de/projects/cdo.

Appendix A: Computation of ERA5 near-surface specific humidity

Significance threshold for a two sided z-test at α=0.1 based on the entire R2B6-CTL simulation. Values for a sample of two-years and two MAM seasons are shown. Autocorrelation is small for precipitation and can be neglected. The near-surface specific humidity q_s, is not included as direct output of ERA5. We derive it via

$$q_s = \frac{0.622\,p_v}{p_s - 0.378\,p_v}. \tag{A1}$$

using the vapour pressure p_v in hPa, which is calculated using ERA5 output of 2-m dew point temperature T_D in Celsius and surface pressure p_s in hPa according to the Magnus formula

$$p_v = 6.112 \times 5\,\exp\left(\frac{17.67\,T_D}{T_D + 243.5\,\mathrm{K}}\right). \tag{A2}$$

Appendix B: Computation of the velocity potential

The velocity potential χ is obtained by computing the inverse Laplacian of the wind field divergence. Specifically, the wind field in the Helmholtz decomposition can be written as

$$\mathbf{u} = \nabla \times \psi - \nabla\chi, \tag{B1}$$

where ψ is the streamfunction. The divergence of the wind field is directly related to χ via

$$\nabla \cdot \mathbf{u} = -\nabla^{\mathbf{2}}\chi, \tag{B2}$$

and $\chi_{l,m}$ in the spectral space can be obtained by calculating the inverse Laplacian in spectral space according to

$$\chi_{l,m=-\frac{r^2 D_{l,m}}{l(l+1)}}, \tag{B3}$$

where $D_{l,m}$ are the spectral coefficients of the wind divergence $\nabla \cdot \mathbf{u}$, r is the earth's radius, l is the zonal wavenumber and m is the longitudinal wavenumber. We analyze χ after transforming back to grid space.

Appendix C: Near-surface humidity biases

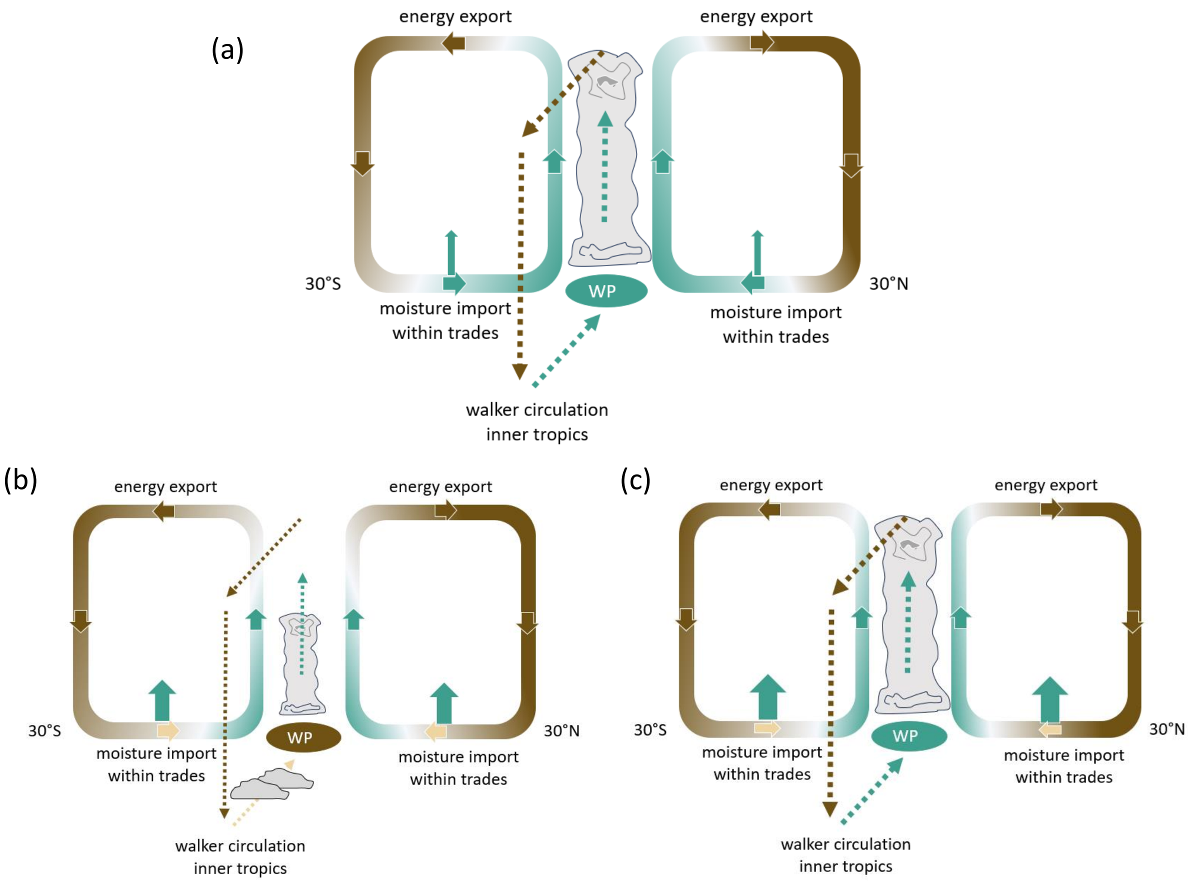

Figure 1. Conceptual depiction of the main zonal and meridional circulations exchanging moisture and energy between the subtropics and the tropics as a) observed, b) in default ICON simulations, and c) in U_{min} adjusted ICON simulations. Observations show that the moisture within the innermost tropics originates from evaporation in tropical and subtropical areas. The moisture is imported into the innermost tropics by the trade winds, with small losses to the free troposphere. In the innermost tropics it is then transported to the main convective regions, i.e., the Warm Pool (WP) within the zonally anomalous Walker circulation. Energy is exported to the subtropics within the outward branches of the Hadley circulation. In conventional ICON simulations (b), a large portion of the subtropical moisture is lost due to too much vertical transport of moisture from the boundary layer to the free troposphere. This leads to a moisture deficit in the tropics, specifically over the WP, reducing deep convection, slowing down the Walker circulation and leading to spurious additional convective centers over the Eastern Pacific as too little moisture is transported to the WP within the boundary layer. In the U_{min} adjusted ICON simulations (c) increased evaporation leads to an additional moisture source in the tropics, which resolves the dry bias over the WP. However, the adjustments increase the positive free-tropospheric moisture bias between $0^{\circ}$to 30°, reduce the trade wind strength and change the balance between innermost-tropical and subtropical sources of tropical moisture content. Green colors indicate high moisture content. Brown colors low moisture content.

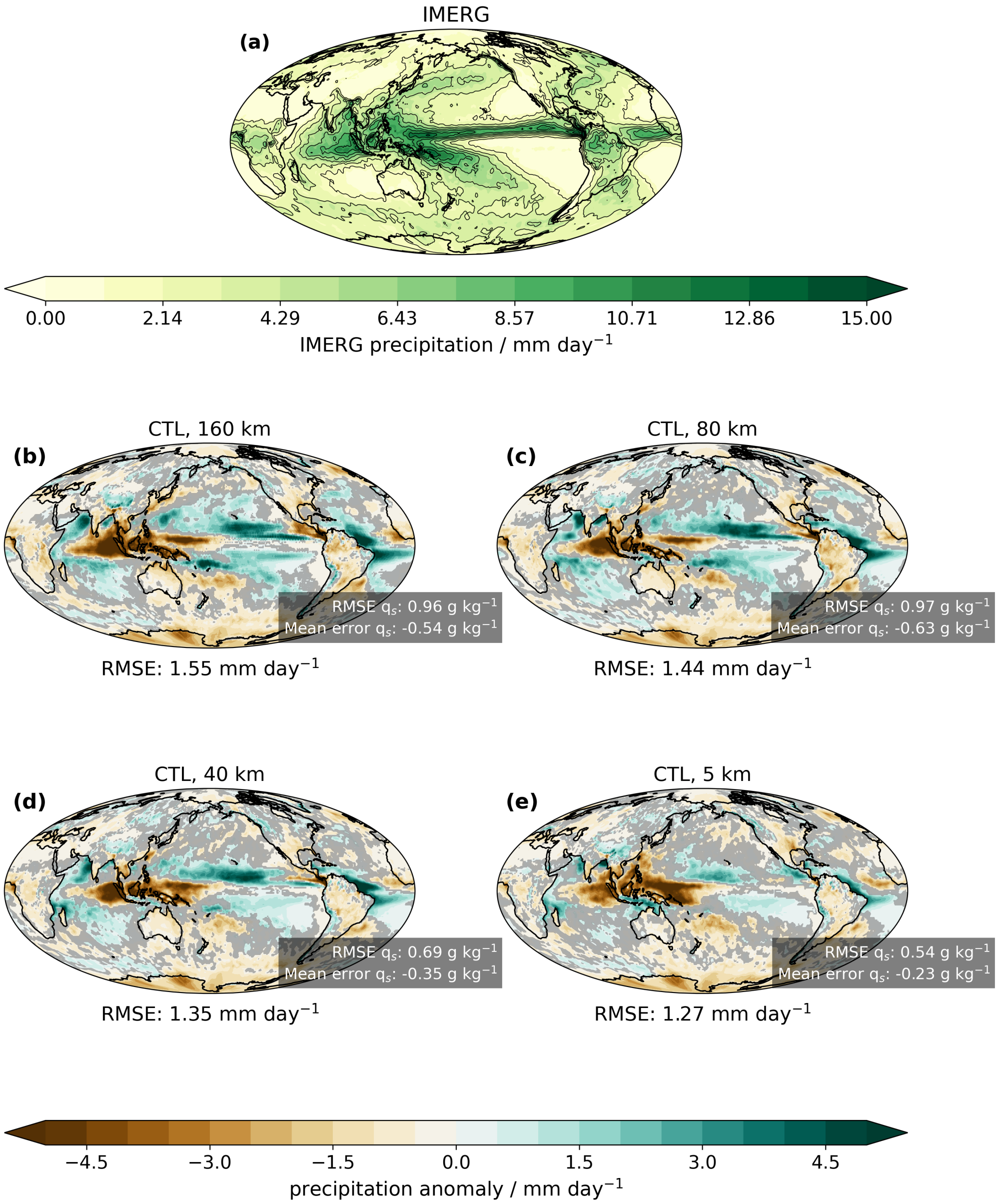

Figure 2. (a) Climatological IMERG precipitation distribution from 2004 to 2010 and (b)-(e) two-year mean precipitation bias with respect to IMERG for 160 km (b), 80 km (c), 40 km (d) and 5 km (e) setups. Statistically insignificant differences between IMERG and the experiments based on a two sided z-test at α=0.1 are grayed out in (b)-(e). The corresponding global RMSE in precipitation is stated beneath the panel for each resolution experiment. The global RMSE and mean error in near-surface specific humidity, calculated with respect to values derived from ERA5 reanalysis, is depicted in the inlays.

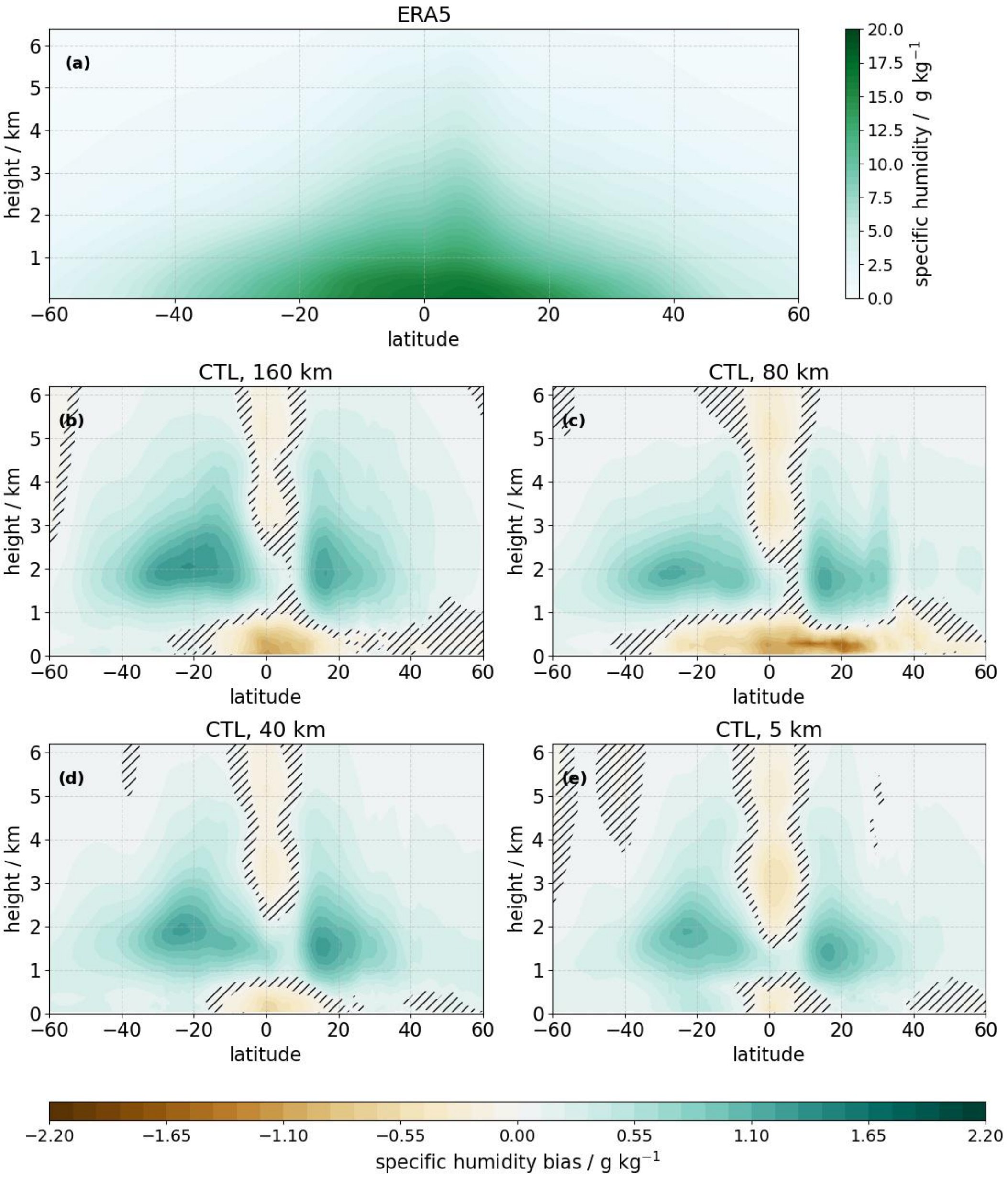

Figure 3. (a) Climatological zonal-mean atmospheric specific humidity distribution from ERA ERA5 for the years 2004 to 2010 and (b)-(e) two-year atmospheric specific humidity bias with respect to ERA5 for R2B4 (160 km (b), R2B5 (80 km (c), R2B6 (40 km (d) and R2B9 (5 km) setups. Statistically significant differences between ERA5 and the model data are shown, and insignificant regions are dashed out.

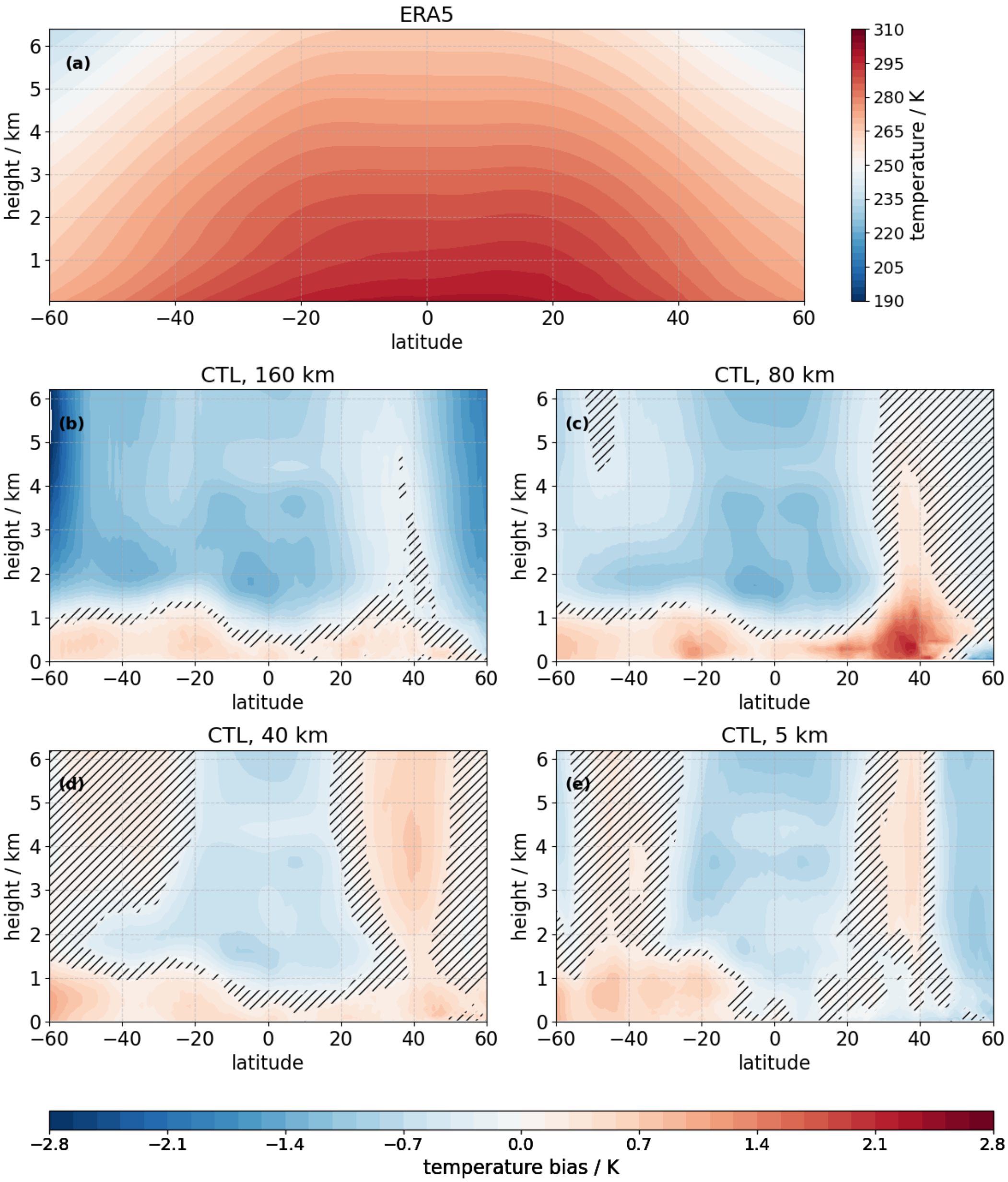

h

Figure 4. (a) Climatological ERA5 zonal zonal-mean temperature fields from ERA5 averaged over the timeframe from 2004 to 2010 and (b)-(e) two-year atmospheric temperature bias with respect to ERA5 for R2B4 (160 km (b), R2B5 (80 km (c), R2B6 (40 km (d) and R2B9 (5 km (e) setups. Statistically significant differences between ERA5 and the model data are shown, insignificant regions are dashed out.

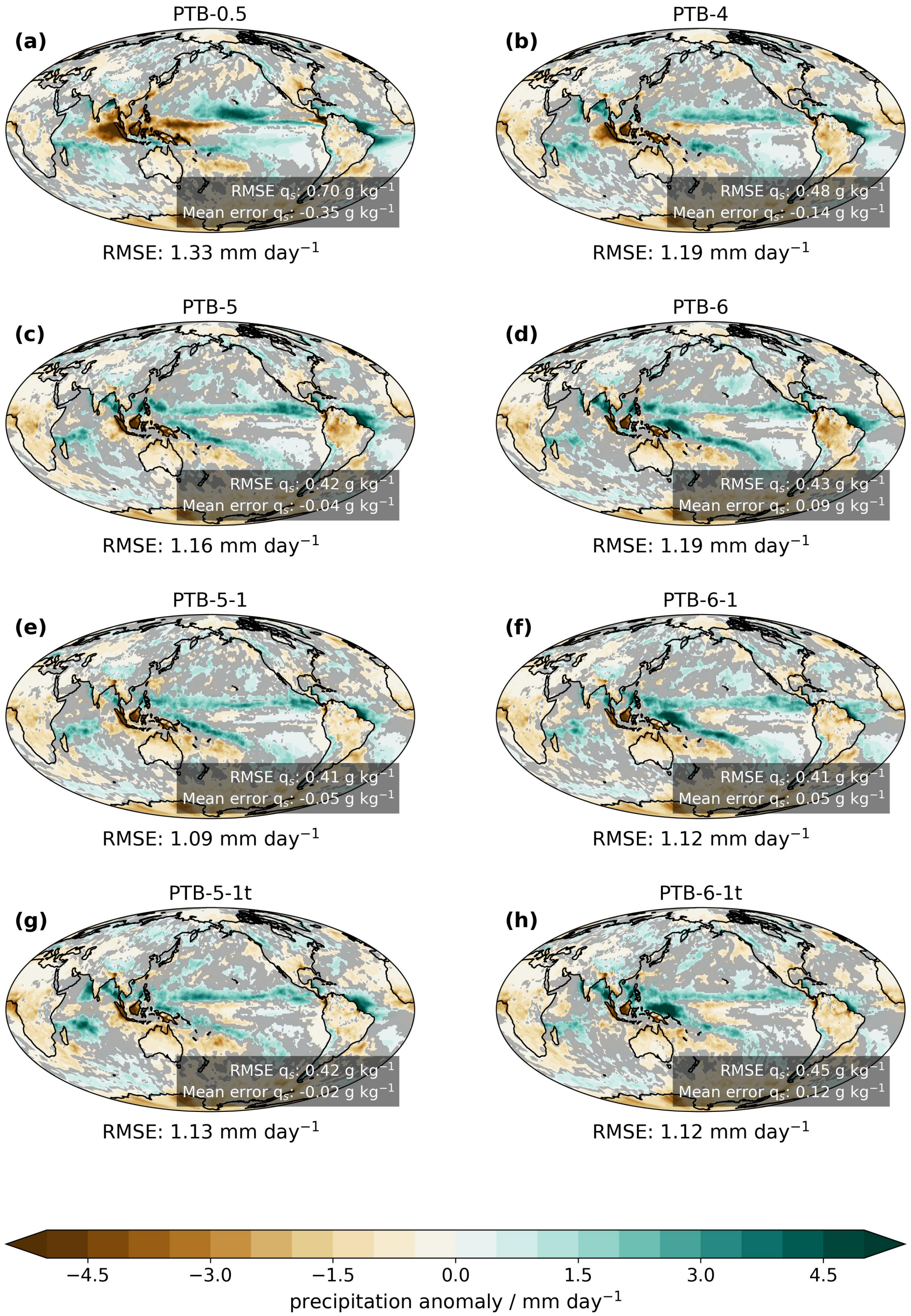

Figure 5. Two-year mean large-scale precipitation bias with respect to IMERG averaged over 2004-2010 for different settings of the surface wind at 40 km resolution: PTB-0.5 (a), PTB-4 (b), PTB-5 (c), PTB-5_1 (e), PTB-5_1t (g), PTB-6 (d), PTB-6_1 (f) and PTB-6_1t (h). The corresponding global precipitation RMSE is stated beneath the panel for each sensitivity experiment. Statistically insignificant differences between IMERG and the experiments based on a two-sided z-test at $\alpha = 0.1$ are grayed out. The global RMSE and mean error in near-surface specific humidity, calculated with respect to values derived from ERA5 reanalysis, is depicted in the inlays.

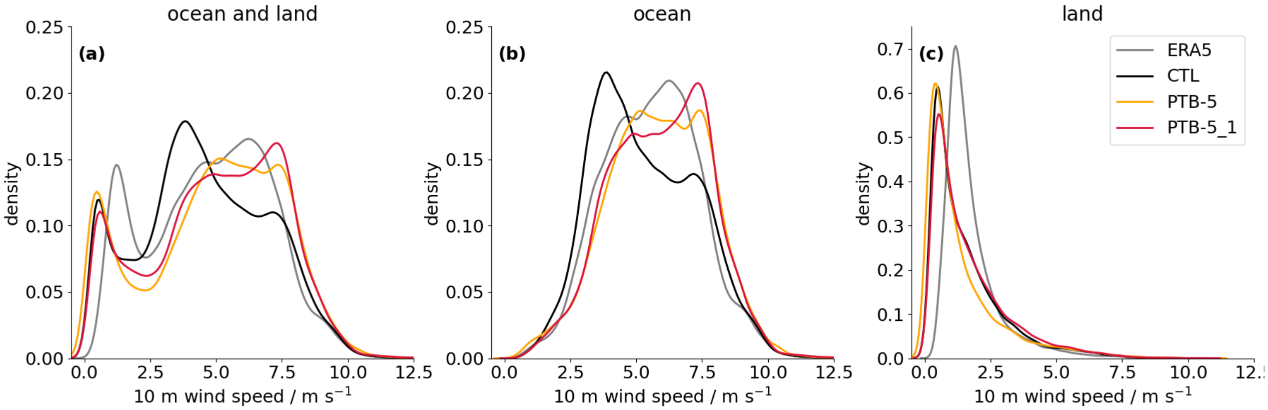

Figure 6. Normalized probability density functions for the monthly mean near-surface wind speed distributions between 10° S to 10° N in the experiments CTL, PTB-5 and PTB-5_1. A comparison with ERA5 data is given for (a) the entire region, (b) over ocean only, and (c) over land only.

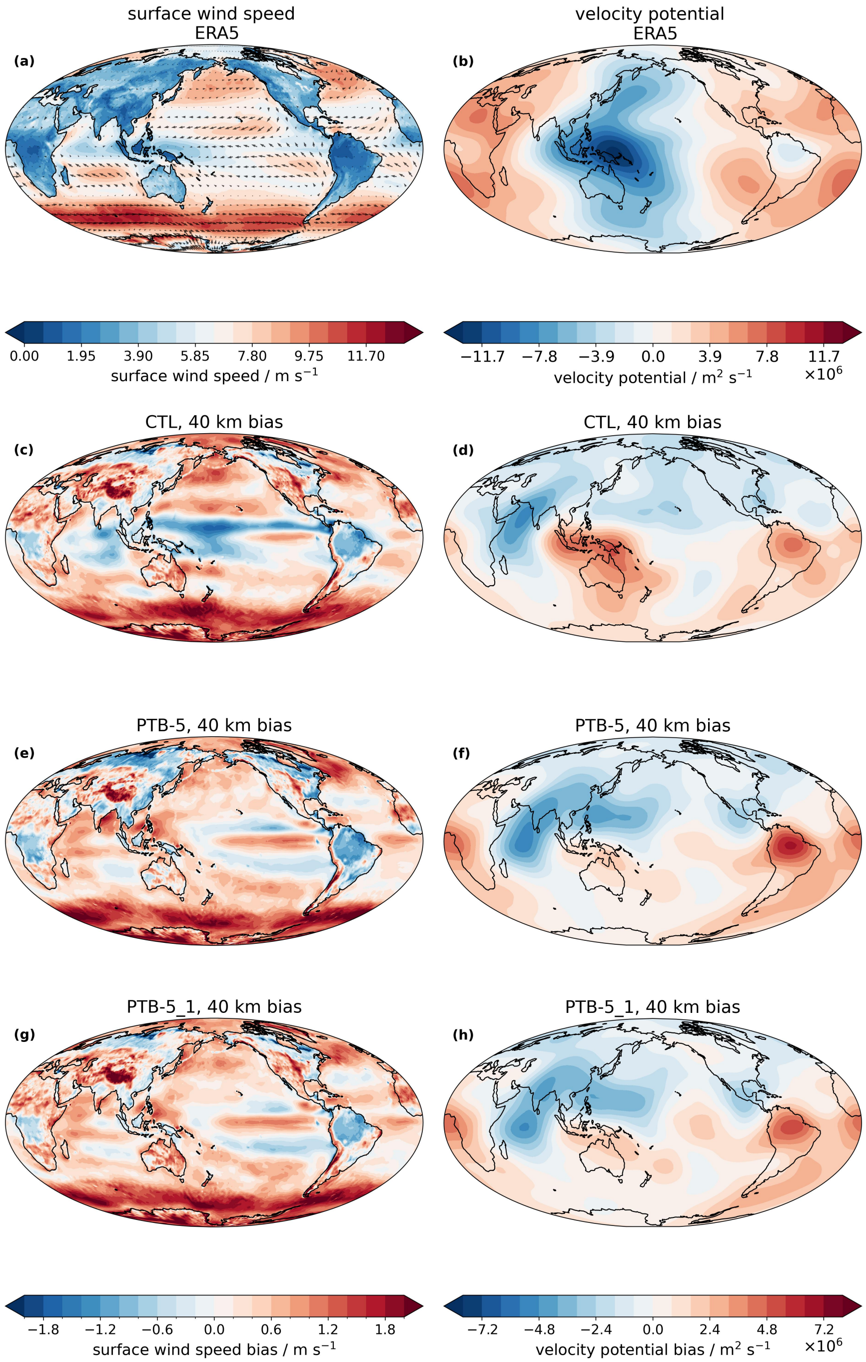

Figure 7. Normalized probability density functions (a) ERA5 multi-year average near surface wind speeds for the zonally averaged monthly mean years 2004-2010. Arrows visualizing the near-surface wind speed distributions between 10° S for ERA5 are superimposed to 10° N in visualize the experiments general circulation. (c, e, g) Two-year mean large-scale near-surface wind speed bias with respect to ERA5 for CTL and different settings of the near-surface wind speed limiter, PTB-5U_{min}, in 40 km resolution : PTB-5_1, PTB-6 and PTB-6PTB-5_1. A comparison with ERA5 data is given for (ab) ERA5 multi-year average velocity potential χ at 200 hPa for the entire region, years 2004-2010. (bd,f,h) over sea onlyTwo-year mean bias of the CTL, PTB-5 and (c) over land onlyPTB-5_1 experiment with respect to the ERA5 velocity potential. Negative values of the velocity potential are found in regions of ascent and divergent motion; positive values in region of subsidence and convergence.

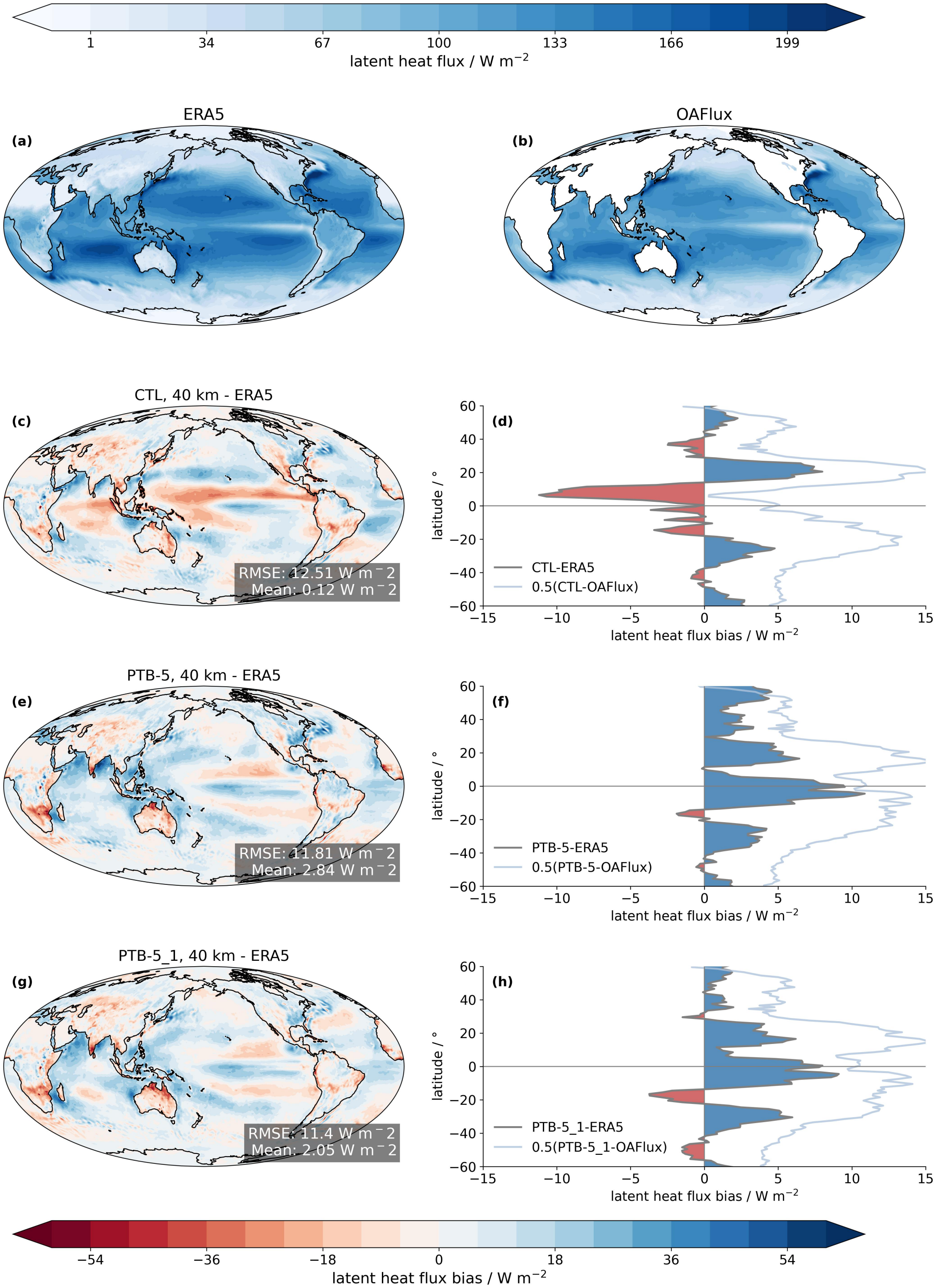

Figure 8. Latent heat flux in reanalysis and 40 km simulations. (a) ERA5 multi-year average latent heat flux for the years 2004-2010. (b) OAFlux multi-year average latent heat flux for the years 2004-2010. Two-year mean large-scale latent heat flux change with respect to ERA for CTL, PTB-5 and PTB-5_1 (c-h). The left column shows global biases, the right column the zonal mean bias with respect to ERA5 (land and ocean) and OAFlux (ocean only).

Latent heat flux in reanalysis and R2B6 simulations. (a) ERA5 multi-year average latent heat flux for the years 2004-2010. (b) OAFlux multi-year average latent heat flux for the years 2004-2010. (c) Two-year mean large-scale latent heat flux change of CTL with respect to ERA5 and OAFlux. (e-j) Two-year mean large-scale latent heat flux change with respect to ERA5 for CTL as well as the different settings of U_{min} in R2B6 (40 km) : PTB-5, PTB-5_1, PTB-5_1t, PTB-6, PTB-6_1 and PTB-6_1t. The root mean square error and mean error with respect to ERA5 are listed in the grey boxes of the graphs (c-j).

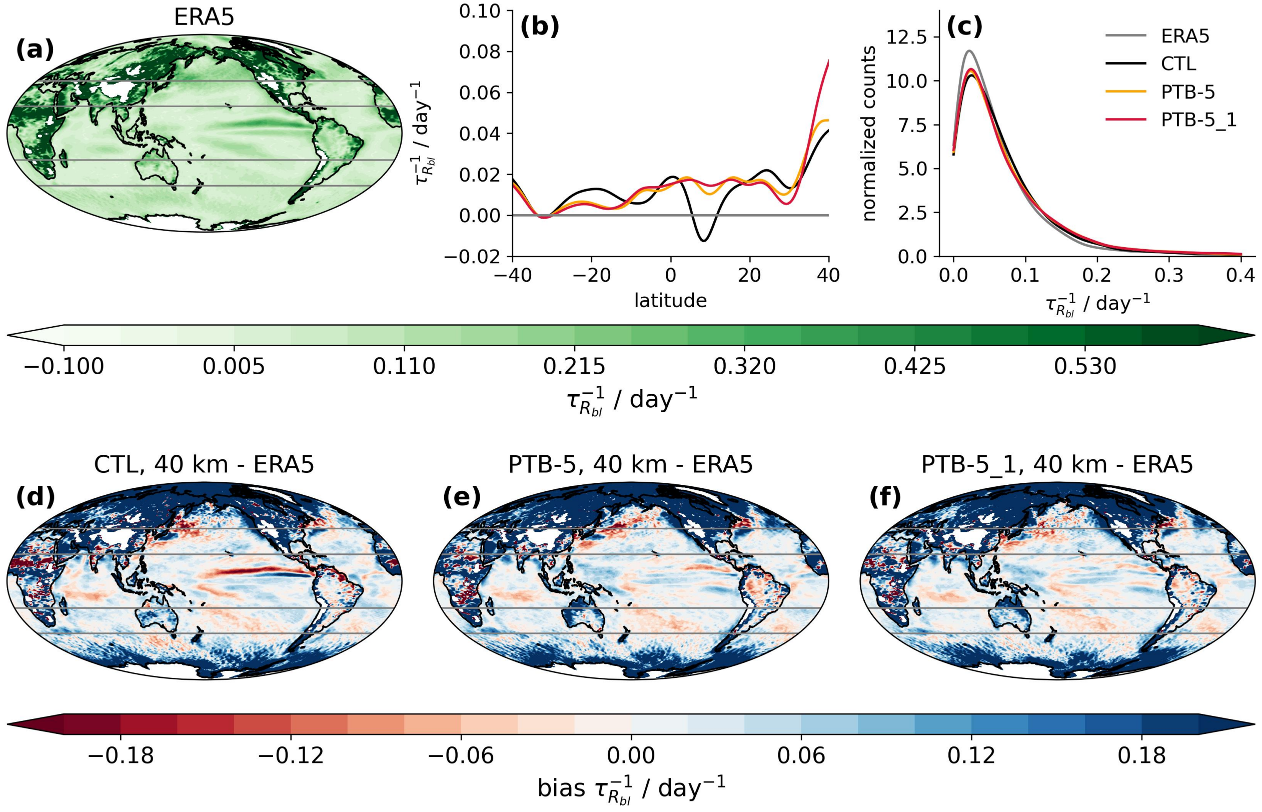

Figure 9. Inverse residence time $\tau_{R_{bl}}$ within the boundary layer up to 850 hPa: (a) ERA5 for the reference years 2004-2010, and differences of two-year average of CTL (d), PTB-5 (e) and PTB-5_1 (f) compared to ERA5. The gray lines mark the 40° and 20° latitudes. (b) Difference of zonal distribution of $\tau_{R_{bl}}$ of CTL, PTB-5 and PTB-5_1 to ERA5 within the latitude band between 40° S and 40° N, restricted to ocean only. (c) Probability density function of $\tau_{R_{bl}}$ of ERA5, CTL, PTB-5 and PTB-5_1 within the latitude band between 40° S and 40° N, restricted to ocean only.

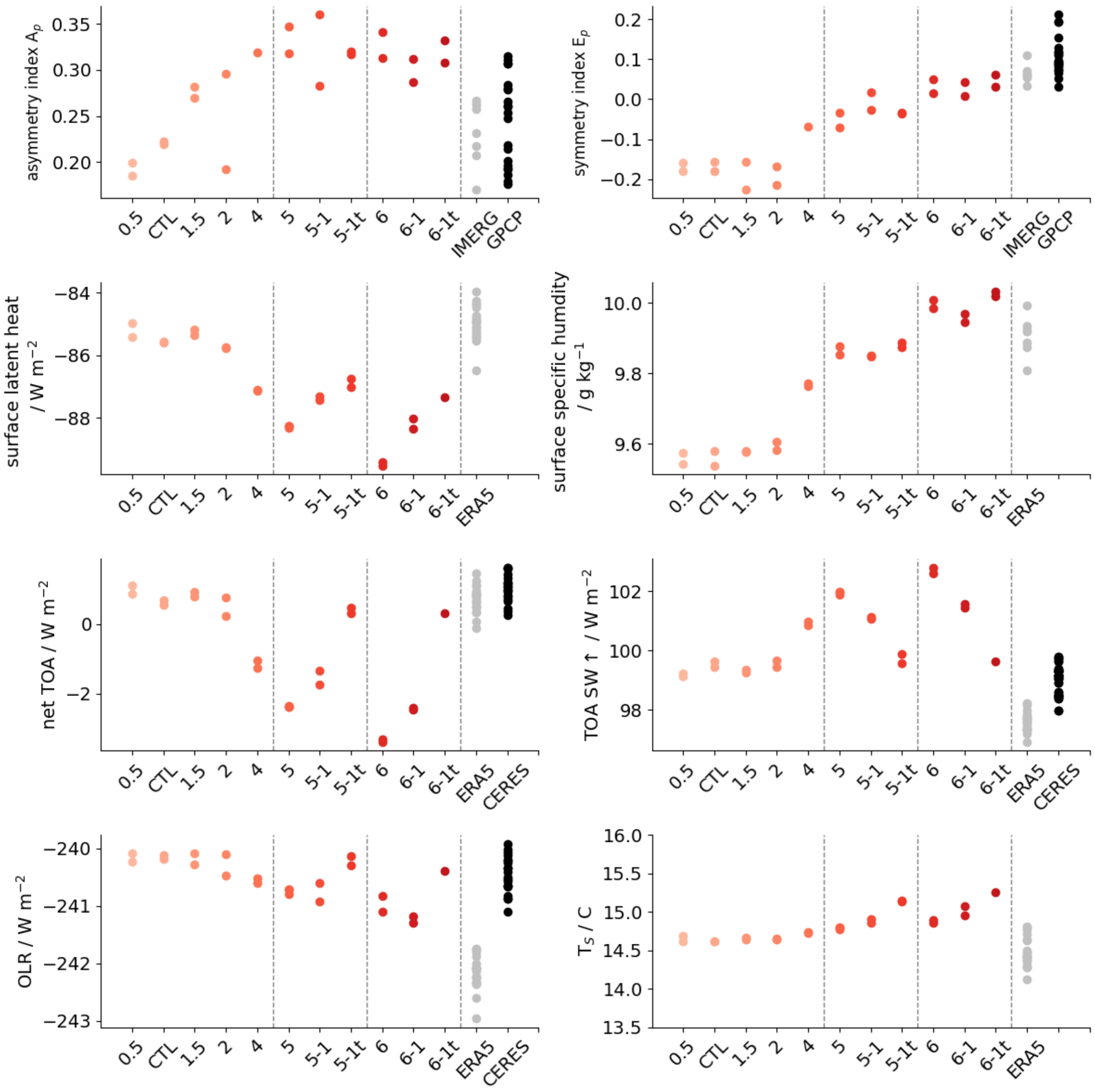

Figure 10. Simulation scores for all 40 km sensitivity experiments as a function of prescribed minimum surface wind speed. The values for a U_{min} of 1 m s^{-1} are the CTL settings and were taken from the respective two years of the CTL simulation. Values for the asymmetric index A_p, symmetry index E_P as well as latent heat flux, near-surface specific humidity q_s, net top-of-the-atmosphere (TOA) imbalance, upwards radiative shortwave flux, outgoing long wave radiation (OLR) and global mean surface temperature T_S are shown. Each point depicts a one-year global average. For reference the corresponding values from IMERG, GPCP, ERA5 and CERES are depicted.

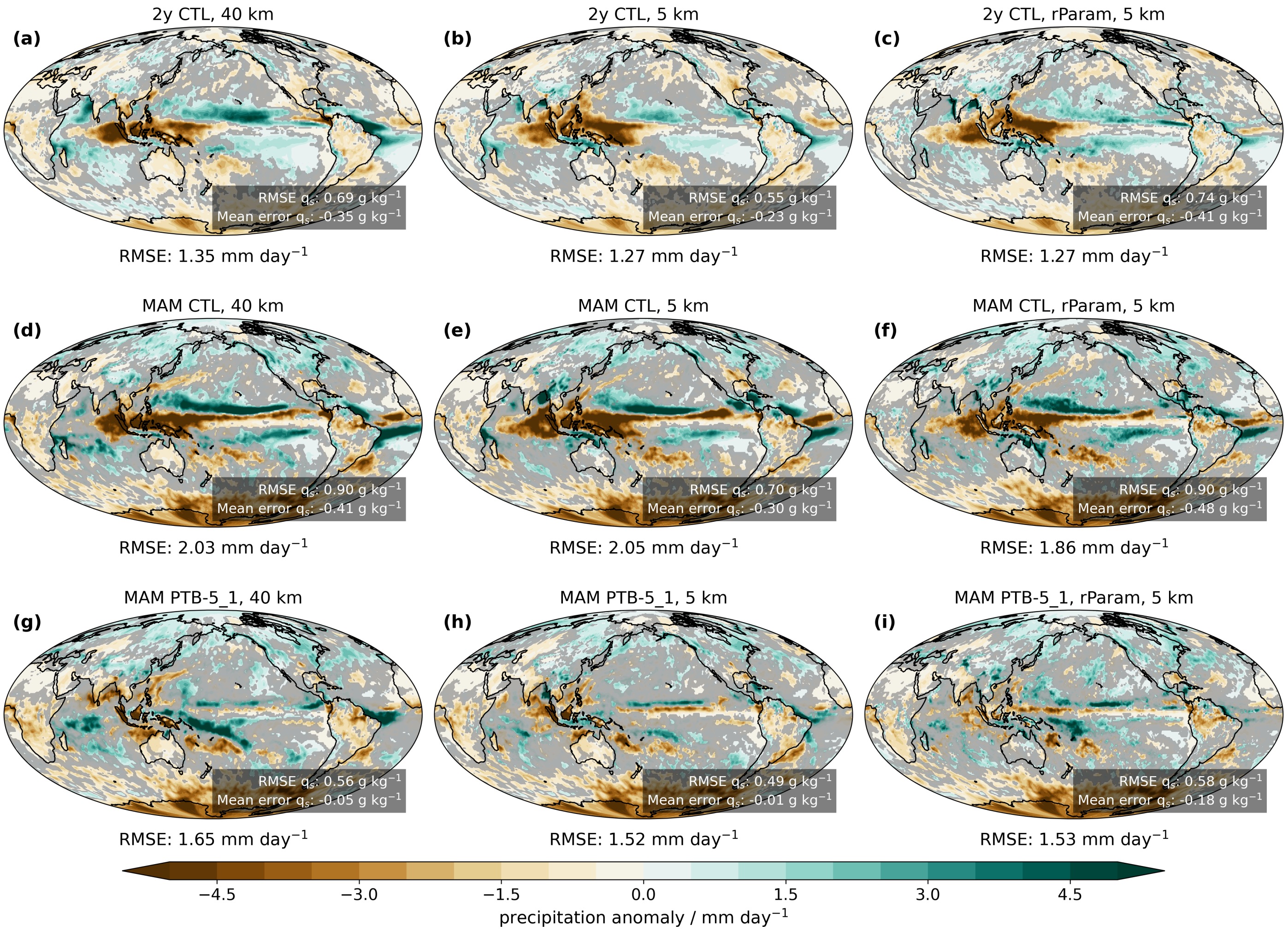

Figure 11. Large-scale precipitation bias with respect to IMERG inthe MAM season: all 2-yr averages from CTL simulations (a-c), PTB-5_1 two-MAM averages from CTL simulations (d-f) and two-MAM averages from PTB-5_1t for R2B6 1 simulations (g-i) for 40 km) and R2B9 (, 5 km). Contours show the IMERG MAM climatologyand 5 km-rParam. The corresponding global precipitation RMSE is stated beneath indicated below the panel for each sensitivity experiment. Statistically insignificant differences between IMERG and the experiments are shown based on a two-sided z-test at $\alpha = 0.1$, and insignificant regions are grayed out. The global RMSE and mean error in the near-surface specific humidity, calculated with respect to the values derived from the ERA5 reanalysisis depicted , are shown in the inlays.

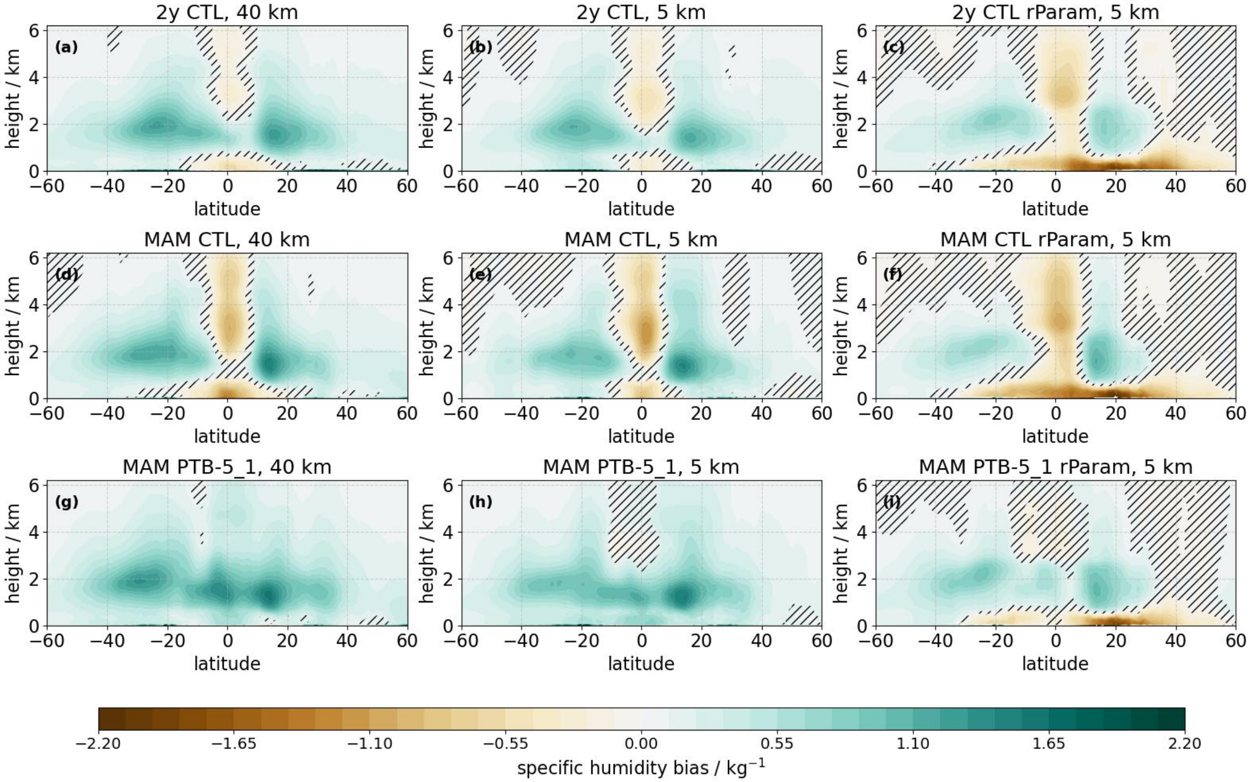

Figure 12. Atmospheric specific humidity bias for two MAM seasons with respect to ERA5: all CTL for R2B6-CTLa 2 year average (a-c), R2B6-PTB-5all CTL for an average over two MAM seasons (d-f) and all PTB-5_1 and R2B6-PTB5-1t for an average over two MAM seasons (g-i) for 40 km) as well as R2B9-CTL, R2B9-PTB-5_1 and R2B9-PTB5-1t (5 km) setupsand 5 km-rParam. Statistically significant differences between ERA5 and the model data are shown, insignificant regions are hatched.

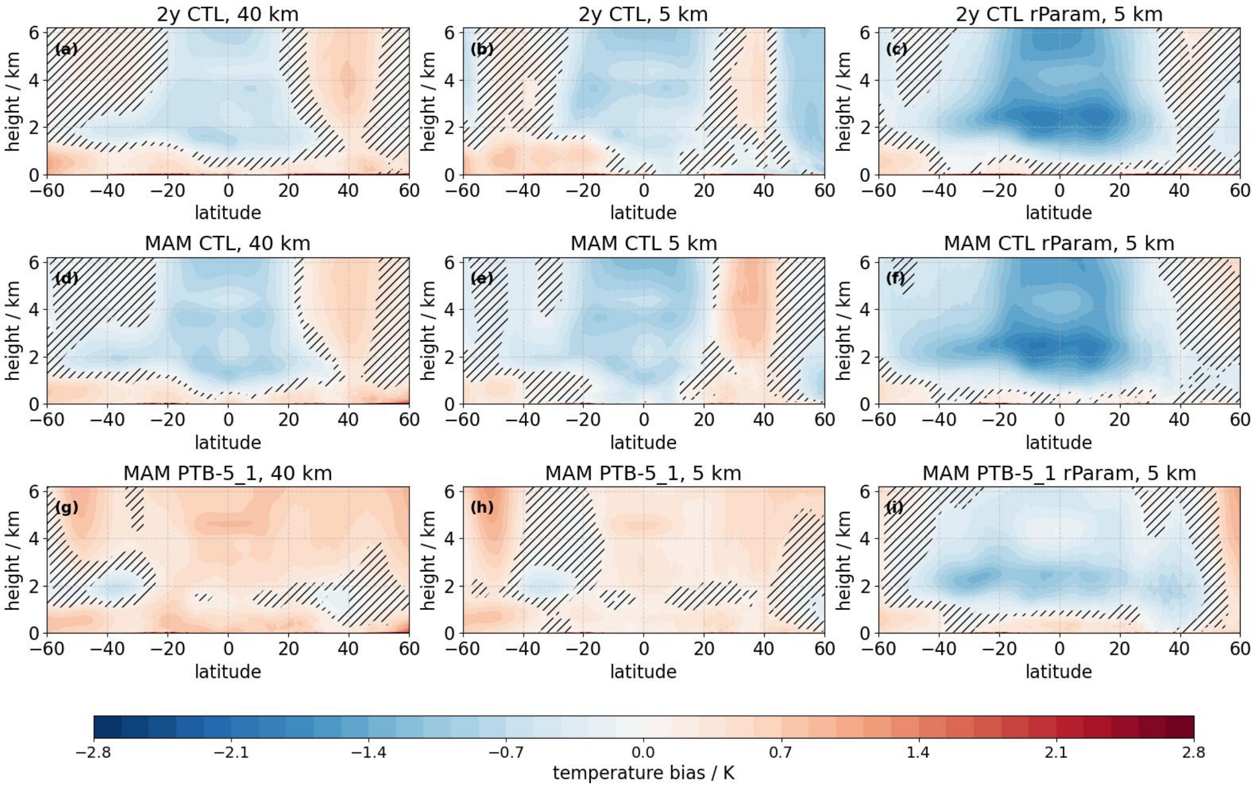

Figure 13. Zonal mean temperature bias for two MAM seasons with respect to ERA5for : all CTL for a 2 year average (a-c), PTB-5_1 all CTL for an average over two MAM seasons (d-f) and all PTB-5_1t in R2B6 1 for an average over two MAM seasons (g-i) for 40 km) as well R2B9 (, 5 km) setupsand 5 km-rParam. Statistically significant differences between ERA5 and the model data are shown, insignificant regions are hatched.

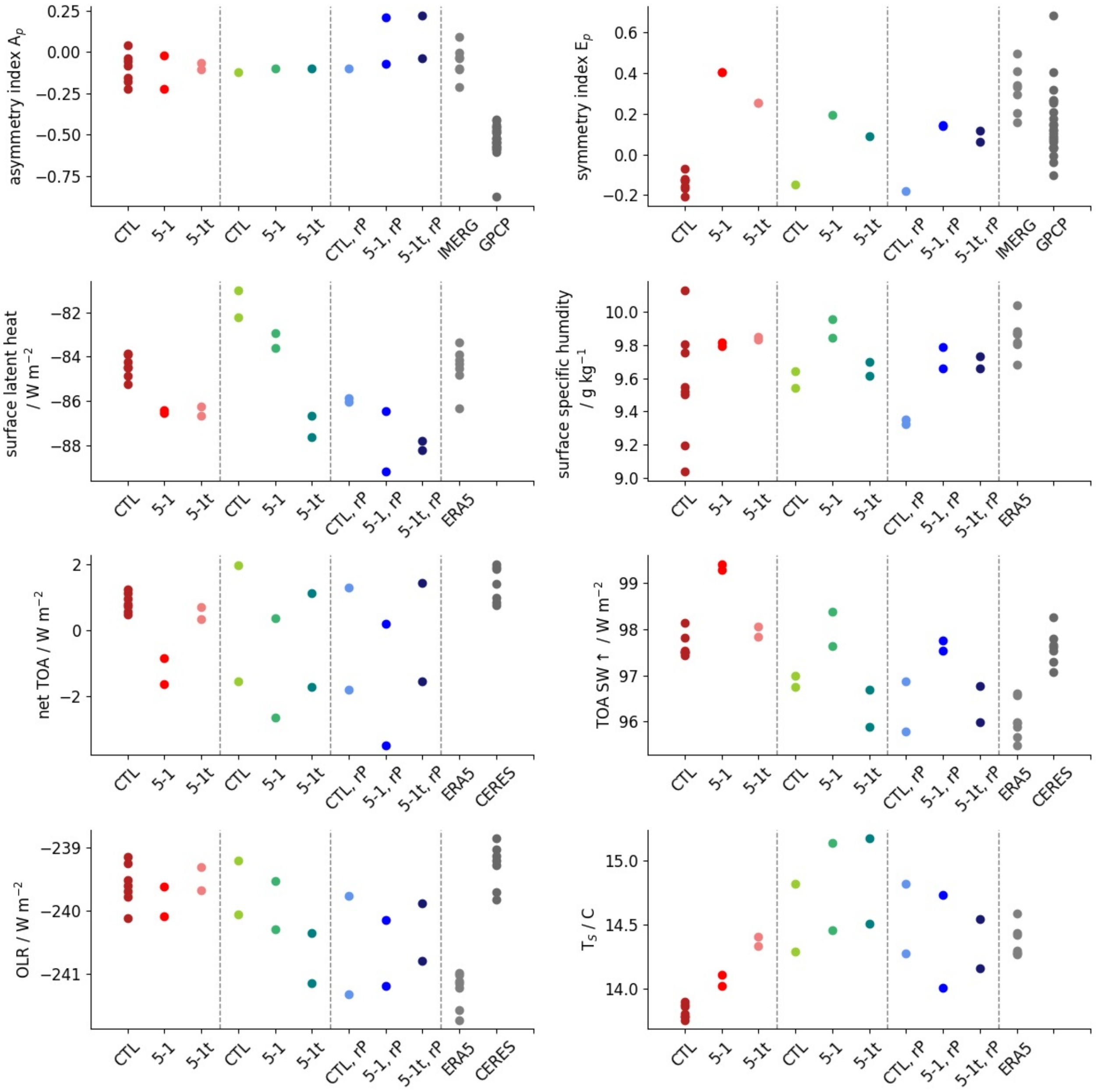

Figure 14. Tuning Simulation scores for two MAM seasons of the R2B6 (40 km) and R2B9 (5 km) CTLas well as their , PTB-5_1 and PTB-5_1t sensitivity experiments in the 40 km, 5 km and 5 km-rParam setup. The R2B6 (40 km) scores are shown in different shades of red, the R2B9 (5 km) setups in shades of green and the 5 km-rParam in different shades of blue. Values for the asymmetric index A_p, symmetry index E_P as well as latent heat flux, near-surface specific humidity q_s, net top-of-the-atmosphere (TOA) imbalance, upwards radiative shortwave flux, outgoing long wave radiation (OLR) and global mean surface near-surface temperature T_S are shown. Each point depicts a one season average. For reference the corresponding values from IMERG, GPCP, ERA5 and CERES are listed.

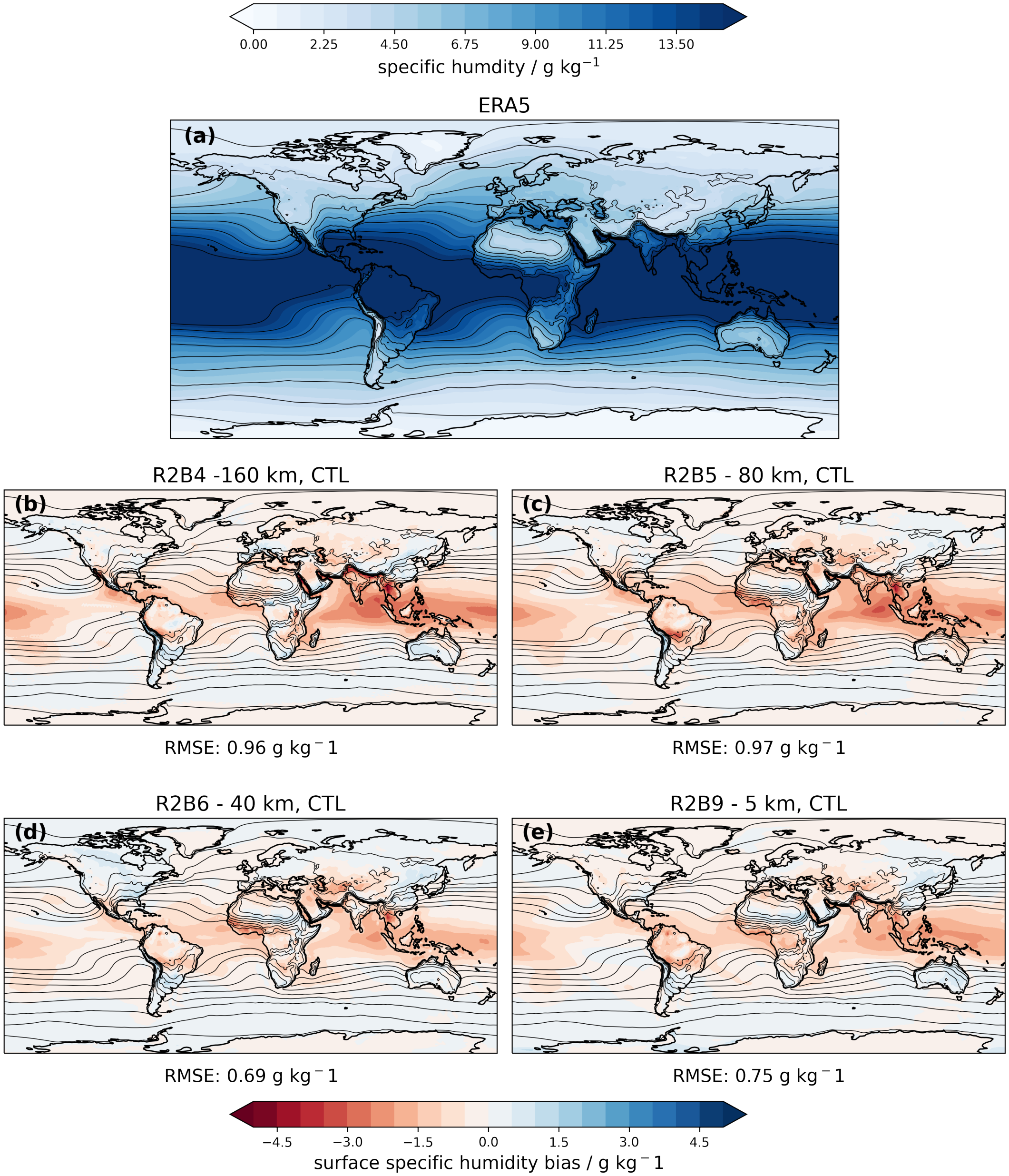

Figure C1. Two-year mean large-scale surface specific humidity bias with respect to ERA5 (2004-2010) over the resolution hierarchy. Global mean root mean square errors are shown below the plots.

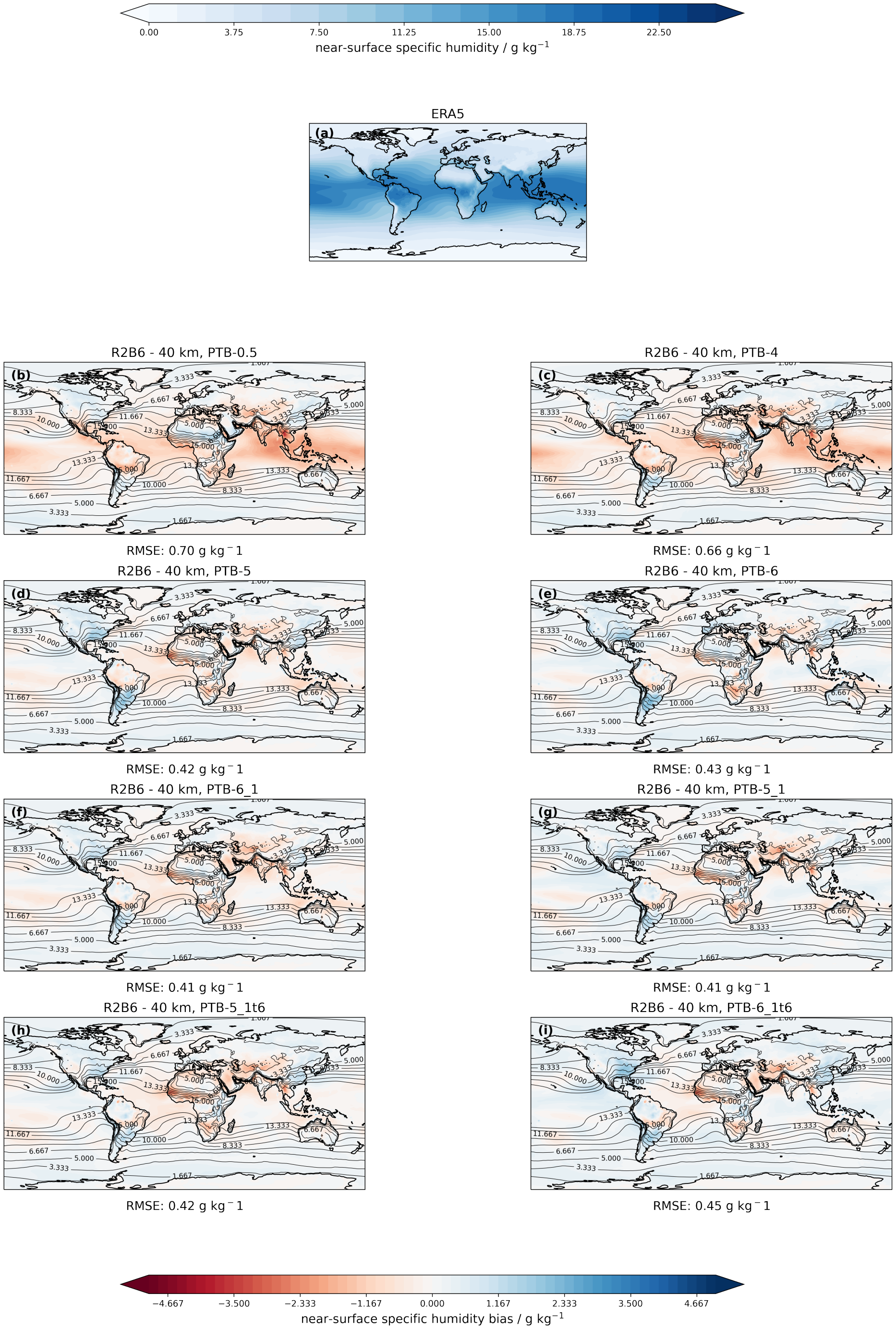

Figure C2. Two-year mean large-scale surface humdity bias with respect to ERA5 (2004-2010) for different settings of the surface wind in R2B6 (40 km): : PTB-0.5, PTB-4, PTB-5, PTB-5_1, PTB-5_1t, PTB-6, PTB-6_1 and PTB-6_1t. Contours show the ERA5 climatology. The corresponding global RMSE is stated beneath the panel for each sensitivity experiment.

Author contributions. CAK had the idea for the study, conceptualized it, acquired computational resources, performed the analysis and wrote the paper manuscript. Model simulations and tuning were done by UN in 160 km, by AS in 80 km and CAK in 40 km and 5 km resolution. RJW provided input on many details of the analysis. LK advised on technical aspects on the model setup and provided the necessary input data. All authors contributed to the interpretation of the results and revised the paper manuscript.

Competing interests. The authors declare that they have no conflict of interest.

Acknowledgements. This research has been supported by the ETH Postdoctoral Fellowship Program (CAK), DWDs Innovation Pro- gramme for Applied Researches and Developments IAFE ICON-Seamless VH 4.7 (AS), the Swiss National Science Foundation Award PCEFP2 203376 (RJW) and the research unit FOR 2820 VolImpact (Grant 398006378) funded by the German Research Foundation (DFG) within the project VOLARC (UN). The authors specifically thank the ICON Seamless/ICON XPP Friends-circle and the XPP Precipitation task force for invaluable collaboration and support throughout the project year. This work greatly benefited from inspiring discussions with our colleagues Kristina Fröhlich, Karel Castro-Morales, Maike Ahlgrimm and Trang van Pham. It would not have been possible to run the ICON XPP code on GPU without Roland Wirth, who fixed some remaining GPU porting bugs. Annika Lauber, Jonas Jucker and Michael Jähn from the C2SM team at ETH have been a great discussion contacts for technical issues encountered around ICON. We thank Doris Folini for insightful scientific discussion with the authors. Computing and data storage resources for the ~~R2B6 and R2B9~~ 40 km and 5 km simulations, were provided by the Swiss National Supercomputing Center (CSCS) in Lugano via the project: s1283 and lp67 as well as the early-testers access to the vCluster Todi on the new Alps infrastructure. William Sawyer, Christoph Müller as well as the technical staff at CSCS have been very supportive of the ICON community when transitioning to the new Alps computing infrastructure. For the R2B5 simulations we thank the German Weather Services for providing computation resources on their system rts, for the R2B4 simulations, we thank the Deutsches Klima Rechenzentrum (DKRZ) for providing resources granted by its Scientific Steering Committee (WLA) under project ID bm0550. The authors thank two anonymous reviewers for constructive and detailed comments on the preprint version of this work.

References

Adam, O., Schneider, T., Brient, F., and Bischoff, T.: Relation of the doubleITCZ bias to the atmospheric energy budget in climate models, Geophysical Research Letters, 43, 7670–7677, https://doi.org/10.1002/2016GL069465, 2016.

Adam, O., Schneider, T., and Brient, F.: Regional and seasonal variations of the double-ITCZ bias in CMIP5 models, Climate Dynamics, 51, 101–117, https://doi.org/10.1007/s00382-017-3909-1, 2018.

Arakawa, A.: The Cumulus Parameterization Problem: Past, Present, and Future, Journal of Climate, 17, 2493–2525, 2004.

Bechtold, P., K"ohler, M., Jung, T., Doblas-Reyes, F., Leutbecher, M., Rodwell, M. J., Vitart, F., and Balsamo, G.: Advances in simulating atmospheric variability with the ECMWF model: From synoptic to decadal time-scales, Quarterly Journal of the Royal Meteorological Society, 134, 1337–1351, https://doi.org/https://doi.org/10.1002/qj.289, _eprint: https://rmets.onlinelibrary.wiley.com/doi/pdf/10.1002/qj.289, 2008.

Bischoff, T. and Schneider, T.: Energetic Constraints on the Position of the Intertropical Convergence Zone, Journal of Climate, 27, 4937–4951, https://doi.org/10.1175/JCLI-D-13-00650.1, 2014.

Boer, G. J.: Diagnostic Equations in Isobaric Coordinates, Monthly Weather Review, 110, 1801–1820, https://doi.org/10.1175/1520-0493(1982)110<1801:DEIIC>2.0.CO;2, 1982.

Bretherton, C. S. and Smolarkiewicz, P. K.: Gravity Waves, Compensating Subsidence and Detrainment around Cumulus Clouds, Journal of Atmospheric Sciences, 46, 740 – 759, https://doi.org/https://doi.org/10.1175/1520-0469(1989)046<0740:GWCSAD>2.0.CO;2, place: Boston MA, USA Publisher: American Meteorological Society, 1989.

C3S: ERA5 hourly data on single levels from 1940 to present, https://doi.org/10.24381/CDS.ADBB2D47, 2018.

Charney, J. G.: A Note on Large-Scale Motions in the Tropics, Journal of the Atmospheric Sciences, 20, 607–609, https://doi.org/10.1175/1520-0469(1963)020<0607:ANOLSM>2.0.CO;2, 1963.

Clark, J. P., Lin, P., and Hill, S. A.: ITCZ Response to Disabling Parameterized Convection in Global FixedSST GFDLAM4 Aquaplanet Simulations at 50 and 6 km Resolutions, Journal of Advances in Modeling Earth Systems, 16, e2023MS003 968, https://doi.org/10.1029/2023MS003968, 2024.

Dee, D. P., Uppala, S. M., Simmons, A. J., Berrisford, P., Poli, P., Kobayashi, S., Andrae, U., Balmaseda, M. A., Balsamo, G., Bauer, P., Bechtold, P., Beljaars, A. C. M., van de Berg, L., Bidlot, J., Bormann, N., Delsol, C., Dragani, R., Fuentes, M., Geer, A. J., Haimberger, L., Healy, S. B., Hersbach, H., Hólm, E. V., Isaksen, L., K\textbackslashaallberg, P., K"ohler, M., Matricardi, M., McNally, A. P., Monge-Sanz, B. M., Morcrette, J.-J., Park, B.-K., Peubey, C., de Rosnay, P., Tavolato, C., Thépaut, J.-N., and Vitart, F.: The ERA-Interim reanalysis: configuration and performance of the data assimilation system, Quarterly Journal of the Royal Meteorological Society, 137, 553–597, https://doi.org/10.1002/qj.828, 2011.

Doelling, D. R., Loeb, N. G., Keyes, D. F., Nordeen, M. L., Morstad, D., Nguyen, C., Wielicki, B. A., Young, D. F., and Sun, M.: Geostationary Enhanced Temporal Interpolation for CERES Flux Products, Journal of Atmospheric and Oceanic Technology, 30, 1072–1090, https://doi.org/10.1175/JTECH-D-12-00136.1, 2013.

Doelling, D. R., Sun, M., Nguyen, L. T., Nordeen, M. L., Haney, C. O., Keyes, D. F., and Mlynczak, P. E.: Advances in Geostationary-Derived Longwave Fluxes for the CERES Synoptic (SYN1deg) Product, Journal of Atmospheric and Oceanic Technology, 33, 503–521, https://doi.org/10.1175/JTECH-D-15-0147.1, 2016.

Dong, Y., Armour, K. C., Battisti, D. S., and Blanchard-Wrigglesworth, E.: Two-Way Teleconnections between the Southern Ocean and the Tropical Pacific via a Dynamic Feedback, Journal of Climate, 35, 6267–6282, https://doi.org/10.1175/JCLI-D-22-0080.1, 2022.

Durack, P. J. and Taylor, K. E.: PCMDI AMIP SST and sea-ice boundary conditions version 1.1.4, https://doi.org/10.22033/ESGF/INPUT4MIPS.2204, 2018.

Feng, X., Ding, Q., Wu, L., Jones, C., Wang, H., Bushuk, M., and Topál, D.: Comprehensive Representation of TropicalExtratropical Teleconnections Obstructed by Tropical Pacific Convection Biases in CMIP6, Journal of Climate, 36, 7041–7059, https://doi.org/10.1175/JCLI-D-22-0523.1, 2023.

Frierson, D. M. W., Hwang, Y.-T., Fukar, N. S., Seager, R., Kang, S. M., Donohoe, A., Maroon, E. A., Liu, X., and Battisti, D. S.: Contribution of ocean overturning circulation to tropical rainfall peak in the Northern Hemisphere, Nature Geoscience, 6, 940–944, https://doi.org/10.1038/ngeo1987, 2013.

Früh, B., Potthast, R., Müller, W., Korn, P., Brienen, S., Fr"ohlich, K., Helmert, J., K"ohler, M., Lorenz, S., Pham, T. V., Pohlmann, H., Schlemmer, L., Schnur, R., Schulz, J.-P., Sgoff, C., Vogel, B., Wirth, R., and Zängl, G.: ICON-Seamless, the development of a novel Earth System Model based on ICON for time scales from weather to climate, https://doi.org/10.5194/ems2022-292, 2022.

Gonzalez, A. O., Fahrin, F., Magnusdottir, G., Kinsella, A., and Ganguly, I.: We need to simulate more double ITCZs and less southern ITCZs in reanalyses and coupled climate models, https://doi.org/10.22541/essoar.174017095.57302520/v1, 2025.

Ham, Y.-G. and Kug, J.-S.: Effects of Pacific Intertropical Convergence Zone precipitation bias on ENSO phase transition, Environmental Research Letters, 9, 064 008, https://doi.org/10.1088/1748-9326/9/6/064008, 2014.

Hardiman, S. C., Boutle, I. A., Bushell, A. C., Butchart, N., Cullen, M. J. P., Field, P. R., Furtado, K., Manners, J. C., Milton, S. F., Morcrette, C., OConnor, F. M., Shipway, B. J., Smith, C., Walters, D. N., Willett, M. R., Williams, K. D., Wood, N., Abraham, N. L., Keeble, J., Maycock, A. C., Thuburn, J., and Woodhouse, M. T.: Processes Controlling Tropical Tropopause Temperature and Stratospheric Water Vapor in Climate Models, Journal of Climate, 28, 6516 – 6535, https://doi.org/10.1175/JCLI-D-15-0075.1, 2015.

Held, I. M. and Hoskins, B. J.: Large-Scale Eddies and the General Circulation of the Troposphere, in: Advances in Geophysics, vol. 28, pp. 3–31, Elsevier, ISBN 978-0-12-018828-4, https://doi.org/10.1016/S0065-2687(08)60218-6, 1985.

Henderson, S. A., Maloney, E. D., and Son, S.-W.: MaddenJulian Oscillation Pacific Teleconnections: The Impact of the Basic State and MJO Representation in General Circulation Models, Journal of Climate, 30, 4567–4587, https://doi.org/10.1175/JCLI-D-16-0789.1, 2017.

Hersbach, H., Bell, B., Berrisford, P., Hirahara, S., Horányi, A., MuñozSabater, J., Nicolas, J., Peubey, C., Radu, R., Schepers, D., Simmons, A., Soci, C., Abdalla, S., Abellan, X., Balsamo, G., Bechtold, P., Biavati, G., Bidlot, J., Bonavita, M., De Chiara, G., Dahlgren, P., Dee, D., Diamantakis, M., Dragani, R., Flemming, J., Forbes, R., Fuentes, M., Geer, A., Haimberger, L., Healy, S. B., Hogan, R., Hólm, E., Janisková, M., Keeley, S., Laloyaux, P., Lopez, P., Lupu, C., Radnoti, G., de Rosnay, P., Rozum, I., Vamborg, F., Villaume, S., and Thépaut, J.-N.: Fifth generation of ECMWF atmospheric reanalyses of the global climate. Complete ERA5 from 1940: Fifth generation of ECMWF atmospheric reanalyses of the global climate., https://doi.org/10.24381/cds.143582cf, 2017.

Hersbach, H., Bell, B., Berrisford, P., Hirahara, S., Horányi, A., MuñozSabater, J., Nicolas, J., Peubey, C., Radu, R., Schepers, D., Simmons, A., Soci, C., Abdalla, S., Abellan, X., Balsamo, G., Bechtold, P., Biavati, G., Bidlot, J., Bonavita, M., De Chiara, G., Dahlgren, P., Dee, D., Diamantakis, M., Dragani, R., Flemming, J., Forbes, R., Fuentes, M., Geer, A., Haimberger, L., Healy, S., Hogan, R. J., Hólm, E., Janisková, M., Keeley, S., Laloyaux, P., Lopez, P., Lupu, C., Radnoti, G., De Rosnay, P., Rozum, I., Vamborg, F., Villaume, S., and Thépaut, J.: The ERA5 global reanalysis, Quarterly Journal of the Royal Meteorological Society, 146, 1999–2049, https://doi.org/10.1002/qj.3803, 2020.

Hogan, R. J. and Bozzo, A.: A Flexible and Efficient Radiation Scheme for the ECMWF Model, Journal of Advances in Modeling Earth Systems, 10, 1990–2008, https://doi.org/https://doi.org/10.1029/2018MS001364, _eprint: https://agupubs.onlinelibrary.wiley.com/doi/pdf/10.1029/2018MS001364, 2018.

Hohenegger, C., Korn, P., Linardakis, L., Redler, R., Schnur, R., Adamidis, P., Bao, J., Bastin, S., Behravesh, M., Bergemann, M., Biercamp, J., Bockelmann, H., Brokopf, R., Brüggemann, N., Casaroli, L., Chegini, F., Datseris, G., Esch, M., George, G., Giorgetta, M., Gutjahr, O., Haak, H., Hanke, M., Ilyina, T., Jahns, T., Jungclaus, J., Kern, M., Klocke, D., Kluft, L., K"olling, T., Kornblueh, L., Kosukhin, S., Kroll, C., Lee, J., Mauritsen, T., Mehlmann, C., Mieslinger, T., Naumann, A. K., Paccini, L., Peinado, A., Praturi, D. S., Putrasahan, D., Rast, S., Riddick, T., Roeber, N., Schmidt, H., Schulzweida, U., Schütte, F., Segura, H., Shevchenko, R., Singh, V., Specht, M., Stephan, C. C., von Storch, J.-S., Vogel, R., Wengel, C., Winkler, M., Ziemen, F., Marotzke, J., and Stevens, B.: ICON-Sapphire: simulating the components of the Earth System and their interactions at kilometer and subkilometer scales, Geoscientific Model Development Discussions, 2022, 1–42, https://doi.org/10.5194/gmd-2022-171, 2022.

Holton, J. R.: An Introduction to Dynamic Meteorology, Academic Press, Amsterdam, Boston, 4th edition edn., 2004.

Hourdin, F., Mauritsen, T., Gettelman, A., Golaz, J.-C., Balaji, V., Duan, Q., Folini, D., Ji, D., Klocke, D., Qian, Y., Rauser, F., Rio, C., Tomassini, L., Watanabe, M., and Williamson, D.: The Art and Science of Climate Model Tuning, Bulletin of the American Meteorological Society, 98, 589–602, https://doi.org/10.1175/BAMS-D-15-00135.1, 2017.

Hsu, C., DeMott, C. A., Branson, M. D., Reeves Eyre, J., and Zeng, X.: Ocean Surface Flux Algorithm Effects on Tropical IndoPacific Intraseasonal Precipitation, Geophysical Research Letters, 49, e2021GL096 968, https://doi.org/10.1029/2021GL096968, 2022.

Hu, Z., Lamraoui, F., and Kuang, Z.: Influence of Upper-Troposphere Stratification and CloudRadiation Interaction on Convective Overshoots in the Tropical Tropopause Layer, Journal of the Atmospheric Sciences, 78, 2493 – 2509, https://doi.org/10.1175/JAS-D-20-0241.1, 2021.

Huffman, G. J.: GPCP Precipitation Level 3 Monthly 0.5-Degree V3.2, https://doi.org/10.5067/MEASURES/GPCP/DATA304, 2021.

Huffman, G. J., Bolvin, D. T., Nelkin, E. J., and Stocker, J. T.: V06 IMERG Release Notes, https://gpm.nasa.gov/sites/default/files/2020-10/IMERG_V06_release_notes_201006_0.pdf, 2010.

Huusko, L., author = Huusko, Linnea and Þórarinsson, Páll Ágúst and Pyykk"o, Joakim and Svensson, Gunilla, P. ., Pyykk"o, J., and Svensson, G.: Resolution dependence of the turbulent atmospheric boundary layer in global stormresolving climate simulations, Quarterly Journal of the Royal Meteorological Society, p. e4940, https://doi.org/10.1002/qj.4940, 2025.

Hwang, Y.-T. and Frierson, D. M. W.: Link between the double-Intertropical Convergence Zone problem and cloud biases over the Southern Ocean, Proceedings of the National Academy of Sciences, 110, 4935–4940, https://doi.org/10.1073/pnas.1213302110, 2013.

Hájková, D. and ácha, P.: Parameterized orographic gravity wave drag and dynamical effects in CMIP6 models, Climate Dynamics, https://doi.org/10.1007/s00382-023-07021-0, 2023.

Iles, C. E., Vautard, R., Strachan, J., Joussaume, S., Eggen, B. R., and Hewitt, C. D.: The benefits of increasing resolution in global and regional climate simulations for European climate extremes, Geoscientific Model Development, 13, 5583–5607, https://doi.org/10.5194/gmd-13-5583-2020, 2020.

Jeevanjee, N.: Vertical Velocity in the Gray Zone, Journal of Advances in Modeling Earth Systems, 9, 2304–2316, https://doi.org/https://doi.org/10.1002/2017MS001059, _eprint: https://agupubs.onlinelibrary.wiley.com/doi/pdf/10.1002/2017MS001059, 2017.

Jones, T. R. and Randall, D. A.: Quantifying the limits of convective parameterizations, Journal of Geophysical Research: Atmospheres, 116, https://doi.org/https://doi.org/10.1029/2010JD014913, 2011.

Kang, S. M., Held, I. M., Frierson, D. M. W., and Zhao, M.: The Response of the ITCZ to Extratropical Thermal Forcing: Idealized Slab-Ocean Experiments with a GCM, Journal of Climate, 21, 3521–3532, https://doi.org/10.1175/2007JCLI2146.1, 2008.

Kang, S. M., Hawcroft, M., Xiang, B., Hwang, Y.-T., Cazes, G., Codron, F., Crueger, T., Deser, C., Hodnebrog, ., Kim, H., Kim, J., Kosaka, Y., Losada, T., Mechoso, C. R., Myhre, G., Seland, ., Stevens, B., Watanabe, M., and Yu, S.: ExtratropicalTropical Interaction Model

Intercomparison Project (Etin-Mip): Protocol and Initial Results, Bulletin of the American Meteorological Society, 100, 2589–2606, https://doi.org/10.1175/BAMS-D-18-0301.1, 2019.

Lang, T., Naumann, A. K., Buehler, S. A., Stevens, B., Schmidt, H., and Aemisegger, F.: Sources of Uncertainty in Mid-Tropospheric Tropical Humidity in Global Storm-Resolving Simulations, Journal of Advances in Modeling Earth Systems, 15, e2022MS003 443, https://doi.org/https://doi.org/10.1029/2022MS003443, _eprint: https://agupubs.onlinelibrary.wiley.com/doi/pdf/10.1029/2022MS003443, 2023.

Lin, J.-L.: The Double-ITCZ Problem in IPCC AR4 Coupled GCMs: OceanAtmosphere Feedback Analysis, Journal of Climate, 20, 4497–4525, https://doi.org/10.1175/JCLI4272.1, 2007.

Lott, F. and Miller, M. J.: A new subgrid-scale orographic drag parametrization: Its formulation and testing, Quarterly Journal of the Royal Meteorological Society, 123, 101–127, https://doi.org/https://doi.org/10.1002/qj.49712353704, _eprint: https://rmets.onlinelibrary.wiley.com/doi/pdf/10.1002/qj.49712353704, 1997.

Lu, J., Vecchi, G. A., and Reichler, T.: Expansion of the Hadley cell under global warming, Geophysical Research Letters, 34, 2006GL028 443, https://doi.org/10.1029/2006GL028443, 2007.

Ma, X., Zhao, S., Zhang, H., and Wang, W.: The double ITCZ problem in CMIP6 and the influences of deep convection and model resolution, International Journal of Climatology, 43, 2369–2390, https://doi.org/10.1002/joc.7980, 2023.

Magnusdottir, G. and Wang, C.-C.: Intertropical Convergence Zones during the Active Season in Daily Data, Journal of the Atmospheric Sciences, 65, 2425–2436, https://doi.org/10.1175/2007JAS2518.1, 2008.

Marshall, J., Donohoe, A., Ferreira, D., and McGee, D.: The oceans role in setting the mean position of the Inter-Tropical Convergence Zone, Climate Dynamics, 42, 1967–1979, https://doi.org/10.1007/s00382-013-1767-z, 2014.

Martens, B., Schumacher, D. L., Wouters, H., Muñoz-Sabater, J., Verhoest, N. E. C., and Miralles, D. G.: Evaluating the land-surface energy partitioning in ERA5, Geoscientific Model Development, 13, 4159–4181, https://doi.org/10.5194/gmd-13-4159-2020, 2020.

Mauritsen, T., Svensson, G., Zilitinkevich, S. S., Esau, I., Enger, L., and Grisogono, B.: A Total Turbulent Energy Closure Model for Neutrally and Stably Stratified Atmospheric Boundary Layers, Journal of the Atmospheric Sciences, 64, 4113–4126, https://doi.org/10.1175/2007JAS2294.1, 2007.

Mauritsen, T., Stevens, B., Roeckner, E., Crueger, T., Esch, M., Giorgetta, M., Haak, H., Jungclaus, J., Klocke, D., Matei, D., Mikolajewicz, U., Notz, D., Pincus, R., Schmidt, H., and Tomassini, L.: Tuning the climate of a global model, Journal of Advances in Modeling Earth Systems, 4, 2012MS000 154, https://doi.org/10.1029/2012MS000154, 2012.

Mechoso, C., Robertson, A., Barth, N., Davey, M., Delecluse, P., Gent, P., Ineson, S., Kirtman, B., Latif, M., Treut, H. L., Nagai, T., Neelin, J., Philander, S., Polcher, J., Schopf, P., Stockdale, T., Suarez, M., Terray, L., Thual, O., and Tribbia, J.: The Seasonal Cycle over the Tropical Pacific in Coupled OceanAtmosphere General Circulation Models, Monthly Weather Review, 123, 2825–2838, https://doi.org/10.1175/1520-0493(1995)123<2825:TSCOTT>2.0.CO;2, 1995.

Morris, M., Kushner, P. J., Moore, G. W. K., and Mercan, O.: Resolution Dependence of Extreme Wind Speed Projections in the Great Lakes Region, Journal of Climate, 37, 3153–3171, https://doi.org/10.1175/JCLI-D-23-0547.1, 2024.

Müller, W., Lorenz, S., Pham, T. V., Schneidereit, A., Brovkin, V., Brüggemann, N., Chegini, F., Dommenget, D., Fr"ohlich, K., Früh, B., Gayler, V., Haak, H., Hagemann, S., Hanke, M., Ilyina, T., Jungclaus, J., K"ohler, M., Korn, P., Kornblue, L., Kroll, C., Krüger, J., Niemeier, U., Potthast, R., Riddick, T., Pohlmann, H., Polkova, I., Schlund, M., Sgoff, C., Stacke, T., Wirth, R., and Yu, D.: Source code and scripts for publication "The ICON-based coupled Earth System Model for Climate Predictions and Projections (ICON XPP)", https://doi.org/10.17617/3.UUIIZ8, artwork Size: 700, 95479689, 95510314 Pages: 700, 95479689, 95510314, 2024.

Müller, W. A., Früh, B., Korn, P., Potthast, R., Baehr, J., Bettems, J.-M., B"ol"oni, G., Brienen, S., Fr"ohlich, K., Helmert, J., Jungclaus, J., K"ohler, M., Lorenz, S., Schneidereit, A., Schnur, R., Schulz, J.-P., Schlemmer, L., Sgoff, C., Pham, T. V., Pohlmann, H., Vogel, B., Vogel, H., Wirth, R., Zaehle, S., Zängl, G., Stevens, B., and Marotzke, J.: ICON: Towards vertically integrated model configurations for numerical weather prediction, climate predictions and projections, Bulletin of the American Meteorological Society, https://doi.org/10.1175/BAMS-D-24-0042.1, 2025a.

Müller, W. A., Lorenz, S., Pham, T. V., Schneidereit, A., Brokopf, R., Brovkin, V., Brüggemann, N., Chegini, F., Dommenget, D., Fr"ohlich, K., Früh, B., Gayler, V., Haak, H., Hagemann, S., Hanke, M., Ilyina, T., Jungclaus, J., K"ohler, M., Korn, P., Kornblüh, L., Kroll, C., Krüger, J., Castro-Morales, K., Niemeier, U., Pohlmann, H., Polkova, I., Potthast, R., Riddick, T., Schlund, M., Stacke, T., Wirth, R., Yu, D., and Marotzke, J.: The ICON-based Earth System Model for Climate Predictions and Projections (ICON XPP v1.0), https://doi.org/10.5194/egusphere-2025-2473, 2025b.

National Center for Atmospheric Research Staff, E.: The Climate Data Guide: OAFlux: Objectively Analyzed air-sea Fluxes for the global oceans, https://climatedataguide.ucar.edu/climate-data/oaflux-objectively-analyzed-air-sea-fluxes-global-oceans, 2022.

Niemeier, U., Wallis, S., Timmreck, C., Van Pham, T., and Von Savigny, C.: How the Hunga TongaHunga Ha'apai Water Vapor Cloud Impacts Its Transport Through the Stratosphere: Dynamical and Radiative Effects, Geophysical Research Letters, 50, e2023GL106 482, https://doi.org/10.1029/2023GL106482, 2023.

Orr, A., Bechtold, P., Scinocca, J., Ern, M., and Janiskova, M.: Improved Middle Atmosphere Climate and Forecasts in the ECMWF Model through a Nonorographic Gravity Wave Drag Parameterization, Journal of Climate, 23, 5905 – 5926, https://doi.org/https://doi.org/10.1175/2010JCLI3490.1, place: Boston MA, USA Publisher: American Meteorological Society, 2010.

Paccini, L., Hohenegger, C., and Stevens, B.: Explicit versus Parameterized Convection in Response to the Atlantic Meridional Mode, Journal of Climate, 34, 3343–3354, https://doi.org/10.1175/JCLI-D-20-0224.1, 2021.

Pan, L. L., Honomichl, S. B., Kinnison, D. E., Abalos, M., Randel, W. J., Bergman, J. W., and Bian, J.: Transport of chemical tracers from the boundary layer to stratosphere associated with the dynamics of the Asian summer monsoon, Journal of Geophysical Research: Atmospheres, 121, https://doi.org/10.1002/2016JD025616, 2016.

Peixoto, J. P. and Oort, A. H.: Physics of Climate Peixoto, J. P., & Oort, A. H. (1992). Physics of Climate., American Institute of Physics, ISBN 978-0-88318-712-8, 1992.

Peixóto, J. P. and Oort, A. H.: The Atmospheric Branch Of The Hydrological Cycle And Climate, in: Variations in the Global Water Budget, edited by Street-Perrott, A., Beran, M., and Ratcliffe, R., pp. 5–65, Springer Netherlands, Dordrecht, ISBN 978-94-009-6956-8 978-94-009-6954-4, https://doi.org/10.1007/978-94-009-6954-4_2, 1983.

Philander, S. G. H., Gu, D., Lambert, G., Li, T., Halpern, D., Lau, N.-C., and Pacanowski, R. C.: Why the ITCZ Is Mostly North of the Equator, Journal of Climate, 9, 2958–2972, https://doi.org/10.1175/1520-0442(1996)009<2958:WTIIMN>2.0.CO;2, 1996.

Prill, F., Reinert, D., and Zängl, G.: ICON Tutorial - Working with the ICON Model, https://doi.org/10.5676/DWD_pub/nwv/icon_tutorial2023, 2023.

Reick, C. H., Gayler, V., Goll, D., Hagemann, S., Heidkamp, M., Nabel, J. E. M. S., Raddatz, T., Roeckner, E., Schnur, R., and Wilkenskjeld, S.: JSBACH 3 - The land component of the MPI Earth System Model: documentation of version 3.2, p. 4990986, https://doi.org/10.17617/2.3279802, artwork Size: 4990986 Medium: application/pdf Publisher: MPI für Meteorologie Version Number: 1, 2021.

Ren, Z. and Zhou, T.: Understanding the alleviation of Double-ITCZ bias in CMIP6 models from the perspective of atmospheric energy balance, Climate Dynamics, https://doi.org/10.1007/s00382-024-07238-7, 2024.

Schmidt, H., Rast, S., Bao, J., Fang, S.-W., Jimenez-de la Cuesta, D., Keil, P., Kluft, L., Kroll, C., Lang, T., Niemeier, U., Schneidereit, A., Williams, A. I. L., and Stevens, B.: Effects of vertical grid spacing on the climate simulated in the ICON-Sapphire global storm-resolving model, EGUsphere, 2023, 1–34, https://doi.org/10.5194/egusphere-2023-1575, 2023.

Schneider, D. P., Deser, C., Fasullo, J., and Trenberth, K. E.: Climate Data Guide Spurs Discovery and Understanding, Eos, Transactions American Geophysical Union, 94, 121–122, https://doi.org/10.1002/2013EO130001, 2013.

Schneider, T., Bischoff, T., and Haug, G. H.: Migrations and dynamics of the intertropical convergence zone, Nature, 513, 45–53, https://doi.org/10.1038/nature13636, 2014.

Schneider, T., Leung, L. R., and Wills, R. C. J.: Opinion: Optimizing climate models with process knowledge, resolution, and artificial intelligence, Atmospheric Chemistry and Physics, 24, 7041–7062, https://doi.org/10.5194/acp-24-7041-2024, 2024.

Segura, H., Bayley, C., Fievét, R., Gl"ockner, H., Günther, M., Kluft, L., Naumann, A. K., Ortega, S., Praturi, D. S., Rixen, M., Schmidt, H., Winkler, M., Hohenegger, C., and Stevens, B.: A Single Tropical Rainbelt in Global StormResolving Models: The Role of Surface Heat Fluxes Over the Warm Pool, Journal of Advances in Modeling Earth Systems, 17, e2024MS004 897, https://doi.org/10.1029/2024MS004897, 2025.

Seifert, A.: A revised cloud microphysical parameterization for COSMO-LME., http://www.cosmo-model.org, 2008.

Sherwood, S. C., Bony, S., and Dufresne, J.-L.: Spread in model climate sensitivity traced to atmospheric convective mixing, Nature, 505, 37–42, https://doi.org/10.1038/nature12829, 2014.

Si, W., Liu, H., Zhang, X., and Zhang, M.: Double Intertropical Convergence Zones in Coupled OceanAtmosphere Models: Progress in CMIP6, Geophysical Research Letters, 48, e2021GL094 779, https://doi.org/10.1029/2021GL094779, 2021.

Simmons, A., Soci, C., Nicolas, J., Bell, B., Berrisford, P., Dragani, R., Flemming, J., Haimberger, L., Healy, S., Hersbach, H., Horányi, A., Inness, A., Munoz-Sabater, J., Radu, R., and Schepers, D.: ERA5.1: Rerun of the Fifth generation of ECMWF atmospheric reanalyses of the global climate (2000-2006 only)., https://doi.org/10.24381/cds.143582cf, 2020.

Simpson, I. R., McKinnon, K. A., Kennedy, D., Lawrence, D. M., Lehner, F., and Seager, R.: Observed humidity trends in dry regions contradict climate models, Proceedings of the National Academy of Sciences, 121, e2302480 120, https://doi.org/10.1073/pnas.2302480120, 2024.

Song, X. and Zhang, G. J.: The Roles of Convection Parameterization in the Formation of Double ITCZ Syndrome in the NCAR CESM: I. Atmospheric Processes, Journal of Advances in Modeling Earth Systems, 10, 842–866, https://doi.org/10.1002/2017MS001191, 2018.

Song, X., Ning, C., Duan, Y., Wang, H., Li, C., Yang, Y., Liu, J., and Yu, W.: Observed Extreme AirSea Heat Flux Variations during Three Tropical Cyclones in the Tropical Southeastern Indian Ocean, Journal of Climate, 34, 3683–3705, https://doi.org/10.1175/JCLI-D-20-0170.1, 2021.

Takasuka, D., Kodama, C., Suematsu, T., Ohno, T., Yamada, Y., Seiki, T., Yashiro, H., Nakano, M., Miura, H., Noda, A. T., Nasuno, T., Miyakawa, T., and Masunaga, R.: How Can We Improve the Seamless Representation of Climatological Statistics and Weather Toward Reliable Global KScale Climate Simulations?, Journal of Advances in Modeling Earth Systems, 16, e2023MS003 701, https://doi.org/10.1029/2023MS003701, 2024.

Tan, Z., Kaul, C. M., Pressel, K. G., Cohen, Y., Schneider, T., and Teixeira, J.: An Extended EddyDiffusivity MassFlux Scheme for Unified Representation of SubgridScale Turbulence and Convection, Journal of Advances in Modeling Earth Systems, 10, 770–800, https://doi.org/10.1002/2017MS001162, 2018.

Tanaka, H. L., Ishizaki, N., and Kitoh, A.: Trend and interannual variability of Walker, monsoon and Hadley circulations defined by velocity potential in the upper troposphere, Tellus A: Dynamic Meteorology and Oceanography, 56, 250, https://doi.org/10.3402/tellusa.v56i3.14410, 2004.

Tian, B. and Dong, X.: The Double-ITCZ Bias in CMIP3, CMIP5, and CMIP6 Models Based on Annual Mean Precipitation, Geophysical Research Letters 28 April 2020 47(8): e2020GL087232, num Pages: - e2020GL087232, 2020.

Tian, B., Fetzer, E. J., and Teixeira, J.: Assessing the Tropospheric Temperature and Humidity Simulations in CMIP3/5/6 Models Using the AIRS Obs4MIPs V2.1 Data, Journal of Geophysical Research: Atmospheres, 129, e2023JD040 536, https://doi.org/10.1029/2023JD040536, 2024.

Tiedtke, M.: A Comprehensive Mass Flux Scheme for Cumulus Parameterization in Large-Scale Models, Monthly Weather Review, 117, 1779 – 1800, https://doi.org/https://doi.org/10.1175/1520-0493(1989)117<1779:ACMFSF>2.0.CO;2, place: Boston MA, USA Publisher: American Meteorological Society, 1989.

Trenberth, K. E.: Some Effects of Finite Sample Size and Persistence on Meteorological Statistics. Part I: Autocorrelations, Monthly Weather Review, 112, 2359–2368, https://doi.org/10.1175/1520-0493(1984)112<2359:SEOFSS>2.0.CO;2, 1984.

Vergara-Temprado, J., Ban, N., Panosetti, D., Schlemmer, L., and Schär, C.: Climate Models Permit Convection at Much Coarser Resolutions Than Previously Considered, Journal of Climate, 33, 1915 – 1933, https://doi.org/10.1175/JCLI-D-19-0286.1, 2020.

Wild, M.: The global energy balance as represented in CMIP6 climate models, Climate Dynamics, 55, 553–577, https://doi.org/10.1007/s00382-020-05282-7, 2020.

Zhang, H., Deser, C., Clement, A., and Tomas, R.: Equatorial signatures of the Pacific Meridional Modes: Dependence on mean climate state, Geophysical Research Letters, 41, 568–574, https://doi.org/10.1002/2013GL058842, 2014.

Zhang, Y. and Boos, W. R.: An upper bound for extreme temperatures over midlatitude land, Proceedings of the National Academy of Sciences, 120, e2215278 120, https://doi.org/10.1073/pnas.2215278120, 2023.

Zhao, M., Golaz, J., Held, I. M., Guo, H., Balaji, V., Benson, R., Chen, J., Chen, X., Donner, L. J., Dunne, J. P., Dunne, K., Durachta, J., Fan, S., Freidenreich, S. M., Garner, S. T., Ginoux, P., Harris, L. M., Horowitz, L. W., Krasting, J. P., Langenhorst, A. R., Liang, Z., Lin, P., Lin, S., Malyshev, S. L., Mason, E., Milly, P. C. D., Ming, Y., Naik, V., Paulot, F., Paynter, D., Phillipps, P., Radhakrishnan, A., Ramaswamy, V., Robinson, T., Schwarzkopf, D., Seman, C. J., Shevliakova, E., Shen, Z., Shin, H., Silvers, L. G., Wilson, J. R., Winton, M., Wittenberg, A. T., Wyman, B., and Xiang, B.: The GFDL Global Atmosphere and Land Model AM4.0/LM4.0: 2. Model Description, Sensitivity Studies, and Tuning Strategies, Journal of Advances in Modeling Earth Systems, 10, 735–769, https://doi.org/10.1002/2017MS001209, 2018a.

Zhao, M., Golaz, J., Held, I. M., Guo, H., Balaji, V., Benson, R., Chen, J., Chen, X., Donner, L. J., Dunne, J. P., Dunne, K., Durachta, J., Fan, S., Freidenreich, S. M., Garner, S. T., Ginoux, P., Harris, L. M., Horowitz, L. W., Krasting, J. P., Langenhorst, A. R., Liang, Z., Lin, P., Lin, S., Malyshev, S. L., Mason, E., Milly, P. C. D., Ming, Y., Naik, V., Paulot, F., Paynter, D., Phillipps, P., Radhakrishnan, A., Ramaswamy, V., Robinson, T., Schwarzkopf, D., Seman, C. J., Shevliakova, E., Shen, Z., Shin, H., Silvers, L. G., Wilson, J. R., Winton, M., Wittenberg, A. T., Wyman, B., and Xiang, B.: The GFDL Global Atmosphere and Land Model AM4.0/LM4.0: 1. Simulation Characteristics With Prescribed SSTs, Journal of Advances in Modeling Earth Systems, 10, 691–734, https://doi.org/10.1002/2017MS001208, 2018b.

Zhou, W., Leung, L. R., and Lu, J.: Linking Large-Scale Double-ITCZ Bias to Local-Scale Drizzling Bias in Climate Models, Journal of Climate, 35, 7965 – 7979, https://doi.org/https://doi.org/10.1175/JCLI-D-22-0336.1, place: Boston MA, USA Publisher: American Meteorological Society, 2022.

Zängl, G., Reinert, D., Rípodas, P., and Baldauf, M.: The ICON (ICOsahedral Non-hydrostatic) modelling framework of DWD and MPI-M: Description of the non-hydrostatic dynamical core, Quarterly Journal of the Royal Meteorological Society, 141, 563–579, https://doi.org/https://doi.org/10.1002/qj.2378, _eprint: https://rmets.onlinelibrary.wiley.com/doi/pdf/10.1002/qj.2378, 2015.